AN ASSESSMENT OF FACTORS LIMITING TROPICAL CONGESTUS CLOUD-TOP HEIGHTS

A Dissertation

by

SEAN PATRICK CASEY

Submitted to the Office of Graduate Studies of
Texas A&M University
in partial fulfillment of the requirements for the degree of

DOCTOR OF PHILOSOPHY

December 2009

Major Subject: Atmospheric Sciences

AN ASSESSMENT OF FACTORS LIMITING TROPICAL CONGESTUS CLOUD-TOP HEIGHTS

A Dissertation

by

SEAN PATRICK CASEY

Submitted to the Office of Graduate Studies of
Texas A&M University
in partial fulfillment of the requirements for the degree of

DOCTOR OF PHILOSOPHY

Approved by:

Chair of Committee,	Andrew E. Dessler
Committee Members,	Courtney Schumacher
	Ramalingam Saravanan
	Anthony M. Filippi
Head of Department,	Kenneth P. Bowman

December 2009

Major Subject: Atmospheric Sciences

ABSTRACT

An Assessment of Factors Limiting Tropical Congestus Cloud-Top Heights.

(December 2009)

Sean Patrick Casey, B.S., University of Washington; M.S. Texas A&M University

Chair of Advisory Committee: Dr. Andrew E. Dessler

I investigate the capping mechanisms behind mid-level cumulus congestus clouds. Two theories are analyzed using two months (January-February 2007) of collocated data between the Atmospheric InfraRed Sounder (AIRS) onboard *Aqua* and the Cloud Profiling Radar (CPR) onboard *CloudSat*, as well as data from the European Centre for Medium-Range Weather Forecasts (ECMWF) Reanalysis (a, ERA) Interim Reanalysis.

The first theory is that dry, free-tropospheric air caps convection due to increased detrainment of unsaturated air at cloud-top, limiting the cloud's buoyancy. This theory is given credence by the sharp differences in AIRS relative humidity (RH) between three cloud categories separated by CPR cloud-top height. Broad layers are noted where the difference in local RH is statistically significant. Congestus occurs more frequently than deep convective clouds when the free-tropospheric RH is less than 30%. Mean RH from the ERA reanalysis shows that RH increases in the midtroposphere (around 600 hPa) by a specific difference of 3% in RH in the presence of deep clouds, compared to RH in the presence of congestus.

The second theory is that a decreased vertical temperature lapse rate, dT/dp, would slow cloud growth, creating a mode of cloud-top heights at the stable layer as clouds lose buoyancy. The signal for lapse rate changes in the AIRS data, however, is not as strong as the signal for RH differences. Near 600-400 hPa, roughly the region where congestus cloud-top heights are located, no significant difference in lapse rates is noted between congestus and deep clouds; in fact, the mean values suggest that congestus clouds appear in more unstable atmospheres than deep clouds. Only slight differences in temperature and lapse rate are noted in ERA data as well. These results suggest that drier air may play a greater role in limiting congestus cloud-top heights than increased atmospheric stability.

Five years of relative humidity (RH) observations from the Atmospheric Infrared Sounder (AIRS) instrument aboard the *Aqua* satellite are then analyzed to identify areas of anomalously dry air between 600 and 400 hPa over deep convective regions of the tropical oceans. Back trajectories are then calculated for each observed parcel.

DEDICATION

To my partner, Jim

ACKNOWLEDGEMENTS

I would first like to thank my committee chair, Dr. Andrew E. Dessler, for his guidance and support, as well as assistance in familiarizing myself with the Aqua/AIRS, CloudSat/CPR and CALIPSO/CALIOP data used in this study. Also, I'd like to thank Dr. Courtney Schumacher, Dr. Ramalingam Saravanan, and Dr. Anthony M. Filippi for providing guidance as members of my dissertation committee. Dr. Sun Wong at Texas A&M, and Drs. Eric Fetzer, Gerald Manipon, and Evan Fishbein at the Jet Propulsion Laboratory (JPL) in Pasadena, CA also provided much help with the AIRS data. Dr. Kenneth Bowman gave assistance with the backtrajectory code. Dr. Paul Ciesielski at Colorado State University (CSU) and Dr. Brian Mapes at the University of Miami helped with the Raymond-Blyth buoyancy-sorting model. Dr. Paquita Zuidema at the University of Miami provided the TOGA-COARE mean radiosonde profile, as well as advice on a preliminary draft of a dry air layer paper based on some of the information in this dissertation. Finally, many thanks to Brian Kahn for providing the AIRS/CloudSat collocation code to create the support-product files.

This work was supported by the NASA Earth System Science Fellowship and NASA grants NNX07AR12G and NNX08AR27G, both to Texas A&M University. Many thanks to the Texas A&M Research Foundation for their assistance with the ESS fellowship. AIRS data was obtained from the Goddard Space Flight Center's (GSFC) Data and Information Services Center (DISC). NCEP Reanalysis Derived data provided

by the NOAA/OAR/ESRL PSD, Boulder, Colorado, USA, from their Web site at http://www.cdc.noaa.gov/.

Finally, I'd like to thank my family and friends for their continual love and support throughout my education. I'm a firm believer that every single person we interact with affects us in some way, and all of you have made me into the person I am today. Great thanks also go to my partner, Jim Smith, whose constant motivation and support kept me going on this dissertation.

Some of the information contained within this dissertation is also contained in an article that will be published in the *Journal of Applied Meteorology and Climatology* in September 2009. Other information is contained in an article that has been submitted to the *Journal of Geophysical Research*, and if accepted, would be in press within the year. Both of these papers are co-written with Andrew Dessler and Courtney Schumacher.

NOMENCLATURE

AIRS	Atmospheric InfraRed Sounder
AWS	Aviation Weather Center
CALIOP	Cloud-Aerosol Lidar with Orthogonal Polarization
CALIPSO	Cloud-Aerosol Lidar and Infrared Pathfinder Satellite Observations
CDF	Cumulative Density Function
CFAD	Contoured Frequency by Altitude Diagram
CPR	Cloud Profiling Radar
DJF	December-January-February
ECMWF	European Centre for Medium-Range Weather Forecasts
ENSO	El Niño-Southern Oscillation
EPIC	East Pacific Investigation of Climate
ERA	ECMWF Reanalysis A
FOV	Field of View
GARP	Global Atmosphere Research Program
GATE	GARP Atlantic Tropical Experiment
GMS	Geostationary Meteorological Satellite
GOES	Geostationary Operational Environmental Satellites
ITCZ	Intertropical Convergence Zone
JJA	June-July-August
MAM	March-April-May

MJO	Madden-Julian Oscillation
NASA	National Aeronautics and Space Administration
NCEP	National Centers for Environmental Prediction
NOAA	National Oceanic and Atmospheric Administration
OLR	Outgoing Longwave Radiation
RH	Relative Humidity
R/V	Research Vessel
S_E	Standard Error
SON	September-October-November
SPCZ	South Pacific Convergence Zone
TOGA COARE	Tropical Ocean Global Atmosphere Coupled Ocean-Atmosphere Response Experiment
USA	United States of America
UTC	Universal Time Constant

TABLE OF CONTENTS

CHAPTER Page

LIST OF FIGURES

FIGURE Page

FIGURE Page

FIGURE Page

LIST OF TABLES

CHAPTER I

INTRODUCTION

Johnson et al. [1999] noted that tropical oceanic convective clouds can be grouped into three categories: shallow cumulus, with cloud-top heights near 2 km; mid-level cumulus congestus clouds, with cloud tops near the 0°C melting level; and deep cumulonimbus clouds, with cloud-tops near the tropopause (see Figure 1). Cumulus congestus in particular has received more attention recently. Kikuchi and Takayabu [2004] identified the given cloud types with stages of the Madden-Julian Oscillation (MJO; Figure 2):

1. 'Suppressed stage' with few clouds
2. 'Shallow convection stage' with shallow clouds
3. 'Developing stage' with cumulus congestus clouds
4. 'Mature stage' with deep convective clouds
5. 'Decaying stage' with anvil clouds

Mapes et al. [2006] noted a preference for congestus clouds prior to peak rainfall events associated with deep convection, similar to Kikuchi and Takayabu [2004]. However, while the capping mechanisms behind shallow and deep convection are well understood [Simpson 1992], Johnson et al. [1999] lacked the data to account for the limiting factors of mid-level congestus cloud-top heights.

This dissertation follows the style of *Journal of Geophysical Research*.

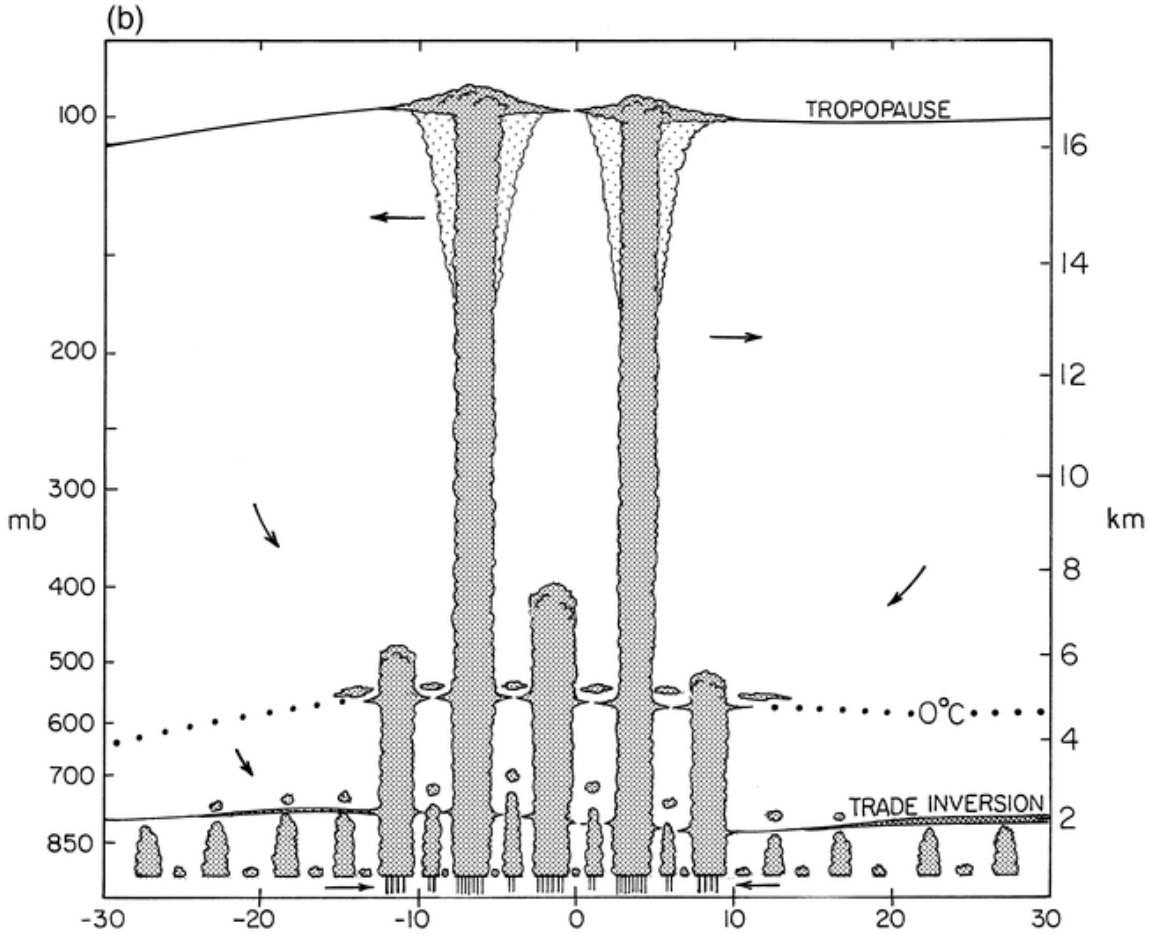

Figure 1. Trimodal distribution of convective clouds (from Johnson et al. [1999]).

One theory focuses on the relation between congestus clouds and a 0°C stable layer [Johnson et al., 1996]. These shallow layers are marked by increased stability in the vertical temperature profile (or inversions in some cases) and a reversal in the specific humidity profile. Johnson et al. [1996] separated these stable layers into two categories: anomalously cool-moist conditions below the 0°C level and anomalously warm-dry conditions above. The anomalously cool-moist conditions occurred within or near precipitating systems, suggesting they were caused by melting ice particles falling

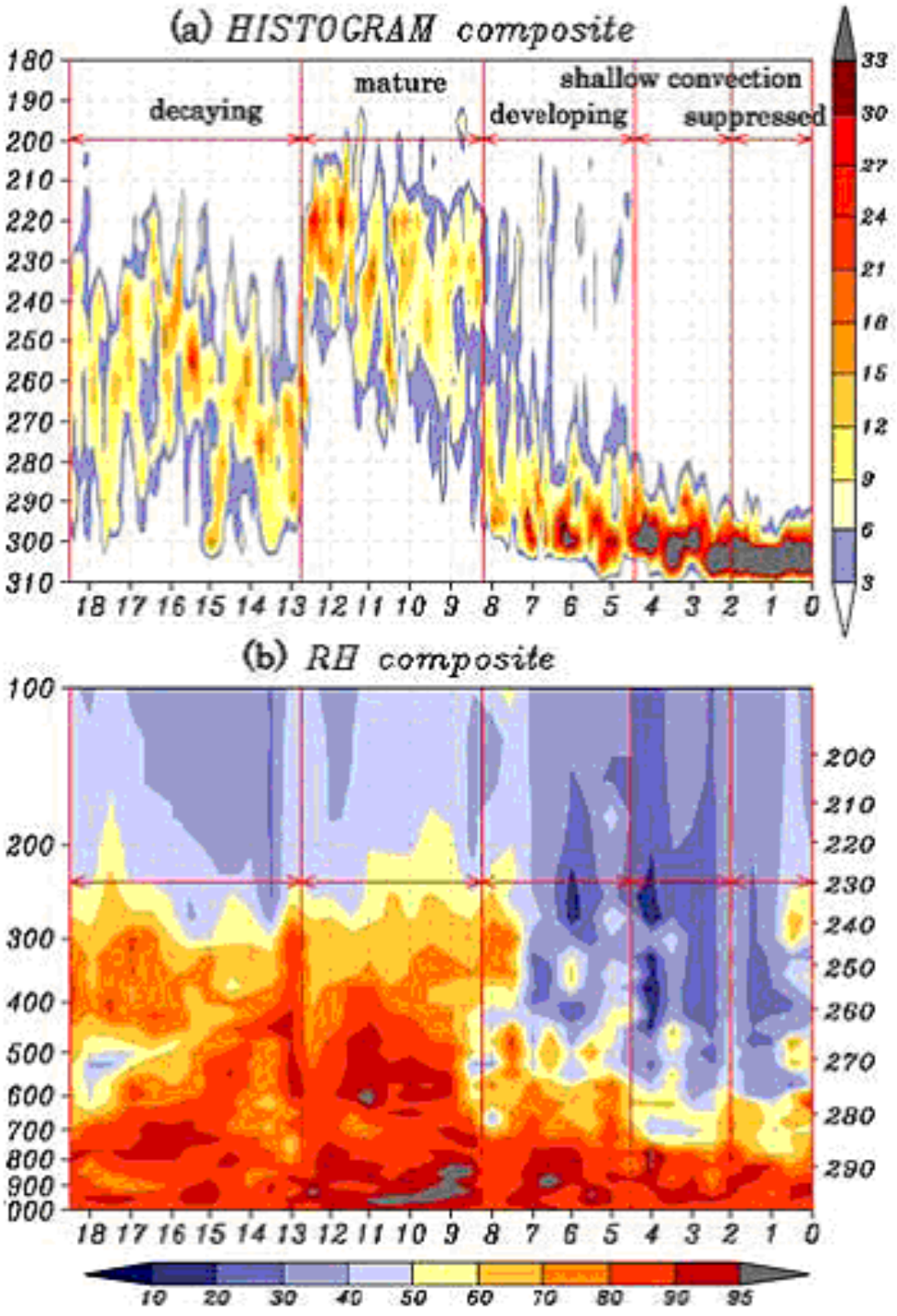

Figure 2. (a) Histogram of brightness temperatures derived from GMS IR TB data over the West Pacific, showing the five stages of cloud development (time right to left); (b) Radiosonde relative humidity composites corresponding to the times in (a). Adapted from Kikuchi and Takayabu (2004).

through the 0°C level. This cools the environment below the melting level, causing an increase in stability. The reasons for anomalously warm-dry conditions are less clear.

While a 0°C stable layer may serve to explain congestus clouds with tops below the 0°C level, it does not explain the capping process behind those congestus clouds with tops above the 0°C level. Zuidema [1998] and Jensen and Del Genio [2006] noted that congestus overshooting this level could begin to glaciate, increasing parcel buoyancy due to latent heat release. This overshooting should allow the cloud to grow to the tropopause; however, clouds sometimes stop growing about one kilometer above the 0°C level.

Another theory for convective cloud capping centers on the effects of layers of anomalously dry air in the tropical midtroposphere. Dry air from aloft in higher latitudes enters the Tropics and subsides in long filaments hundreds of kilometers in width. Yoneyama and Parsons [1999] related these layers to Rossby wave breaking and tracked the source back to mid-latitude baroclinic waves. While the lower and middle atmosphere (below ~8 km) recovered to moist conditions within a week [Parsons et al., 2000], the upper atmosphere (above 8 km) remained anomalously dry for ten to twenty days.

Redelsperger et al. [2002] analyzed the effects of a dry layer observed during the Tropical Ocean Global Atmosphere Coupled Ocean-Atmosphere Response Experiment (TOGA COARE) using a cloud-resolving model. Following the layer's entrance into the study area, moisture in the lower and middle troposphere recovered due to convection penetrating into the dry air mass. The most common mode of convection was congestus

clouds ~4-6 km in height, and the authors suggested that the dry air layer decreased parcel buoyancy, controlling the cloud-top.

Jensen and Del Genio [2006] studied soundings from the Atmospheric Radiation Measurement (ARM) research facility at Nauru Island and analyzed them with a parcel model. This study also showed that a drying of the midtroposphere was more of a factor in limiting congestus cloud-top height than the 0°C stable layer (described in Johnson et al. [1996]). Zuidema et al. [2006] focused on data from the R/V Ronald H. Brown obtained during the 2002 East Pacific Investigation of Climate (EPIC) experiment. This study showed that even outside the west Pacific warm pool, dry air layers were associated with high populations of cumulus congestus clouds. Figure 2b (from Kikuchi and Takayabu [2006]) also shows a marked difference in midtroposphere relative humidity between the developing stage of the MJO, when congestus clouds are frequent, and the mature stage when deep clouds dominate. Kuang and Bretherton [2006] and Khairoutdinov and Randall [2006] also utilized model results to show dry air entrainment acting as a cap to congestus convection.

Despite these modeled results, no study has yet utilized observational evidence to support either the stable layer or the dry-air entrainment theory. This has been difficult, given limitations of high-resolution cloud data required for such a study, in conjunction with large-scale temperature and water vapor measurements. Most oceanic convection is rather small, less than 10 km thick, making their observation and/or resolution in large-scale models nearly impossible. Concurrent with this, atmospheric temperature and water vapor profiles outside of the cloudy area are also necessary, but until recently

have not been available on a concurrent basis. Finally, observations must be able to track the life-cycle of the cloud, not simply apply an instantaneous picture provided by polar-orbiting satellites to the cloud categorization.

This study aims to utilize measurements from NASA's A-Train satellites and global geostationary satellites to analyze the temperature and water vapor signals around active tropical convection, with the goal of finding statistically significant differences in these quantities between cumulus congestus and deep cumulonimbus clouds. Section II looks at identification of convective features using CloudSat and the Cloud-Aerosol Lidar and Infrared Pathfinder Satellite Observations (CALIPSO) satellite. Section III then brings in geostationary satellite data to obtain final cloud-top height, which cannot be determined by the snapshot provided by CloudSat. Section IV introduces the Atmospheric InfraRed Sounder (AIRS) support product and the ECMWF Reanalysis (a, ERA) Interim Reanalysis products, and explains how these are collocated to each identified convective feature. Sections V and VI look at the water vapor and temperature signals, respectively, in the presence of different cloud types using the AIRS and ERA information. Section VII provides an assessment of these results.

. Section VIII describes a methodology for identification of midlevel dry air layers, which may play the main role in limiting congestus development. Section IX analyzes the distribution observed in each ocean basin, along with seasonal separation. Section X uses a back-trajectory model to determine where parcels within these dry air layers were last saturated. Section XI returns to the preceding questions and discusses future areas of research.

CHAPTER II

IDENTIFICATION OF ACTIVE TROPICAL CONVECTION

The potential effects of such dry air anomalies would be most prevalent in deep convective regions over the warm tropical oceans [where the trimodal distribution identified by Johnson et al. (1999) is prevalent]. Therefore, we limit our analysis to oceanic areas where the long-term (1968-1996) monthly mean outgoing longwave radiation (OLR), as measured by NOAA polar-orbiting satellites and obtained from the National Centers for Environmental Prediction (NCEP; Liebmann and Smith 1996), was less than 240 W/m^2. This threshold reduces the study area to only those areas where deep convection is most prevalent (thus lowering the long-term mean OLR), and where the upper atmosphere would be expected to be the most humid given the prevalence of deep convective processes. Figure 3 shows the areas (shaded in gray) for which this criterion holds for the month of January. Much of the west Pacific and Indian Oceans are covered by this range, with smaller portions in the east Pacific and Atlantic Oceans included. During the month of February, the area of low tropical OLR is very similar, with the exception of the east Pacific region shown in Figure 3.

Clouds are then identified using data measured in January-February 2007 from two A-Train satellite instruments. The first is the Cloud Profiling Radar (CPR) instrument onboard CloudSat [Stephens et al. 2002]. The CPR transmits at 94-GHz (W-band) and has a minimum detectable reflectivity of -28 dBZ. It is a nadir-viewing

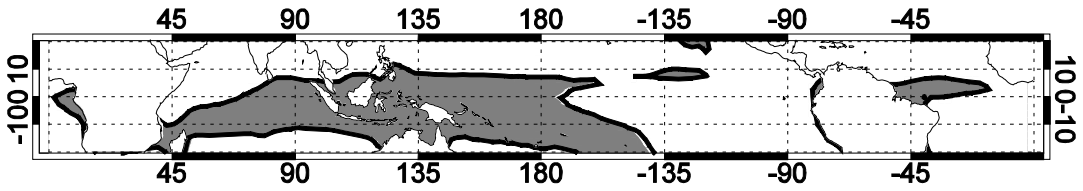

Figure 3. The outline of the locations included in the study (shaded in gray). Thick black line marks the boundary of where the long-term monthly mean OLR for January is less than 240 W/m^2.

instrument with an effective horizontal resolution of 1.4 km. The cloud mask and radar reflectivity product (2B-GEOPROF) will be used in this study.

As this study is only interested in active convection, we want to verify that the cloud features viewed by CloudSat are optically thick. To do this, we utilize the CloudSat 2B-GEOPROF-LIDAR product, which combines CPR data with measurements from the Cloud-Aerosol Lidar with Orthogonal Polarization (CALIOP) instrument onboard the CALIPSO satellite. This product interpolates CALIPSO high-resolution data onto the CloudSat footprint. As CALIPSO passes over the same area 15 seconds after *CloudSat*, the measurements can be assumed to be simultaneous.

Cloud features are identified as those areas in the region shown in Figure 3 that satisfy the following conditions:

1. The cloud is identified as cloud certain (Cloud Mask = 40) by the CPR for the entire depth of the cloud between cloud top and 1 km above the surface.

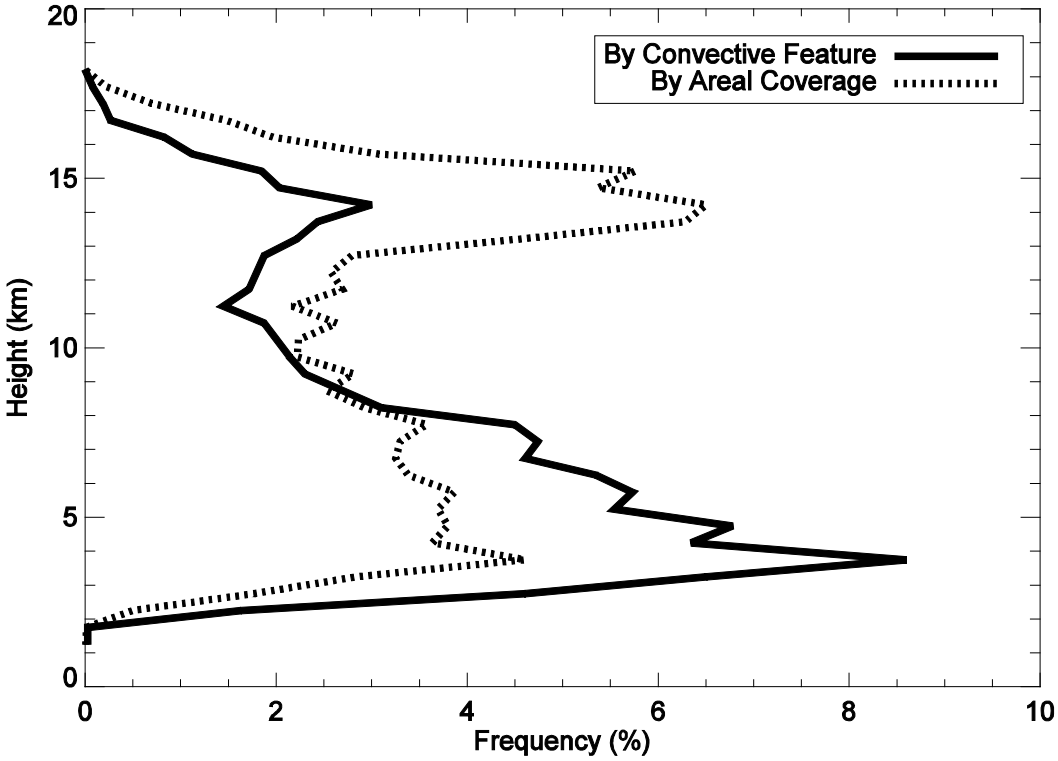

Figure 4. Relative frequency of occurrence of cloud-top heights, binned into 500-m bins. The sum of each data point on each curve adds to unity. Solid line marks the distribution of individual convective features, and dashed line the distribution when size is taken into account.

2. The cloud contains a radar reflectivity of 10 dBZ or higher at some point in its depth, a proxy for precipitation [Luo et al. 2008].
3. CALIPSO-measured cloud-top height is within 1 km of CloudSat-measured cloud-top height; a proxy for an optically thick cloud [Luo et al. 2008].

The requirement that the cloud-top height be greater than 1 km is implied in requirement 1 above. This may have the effect of removing many of the shallow cumulus, as the tops

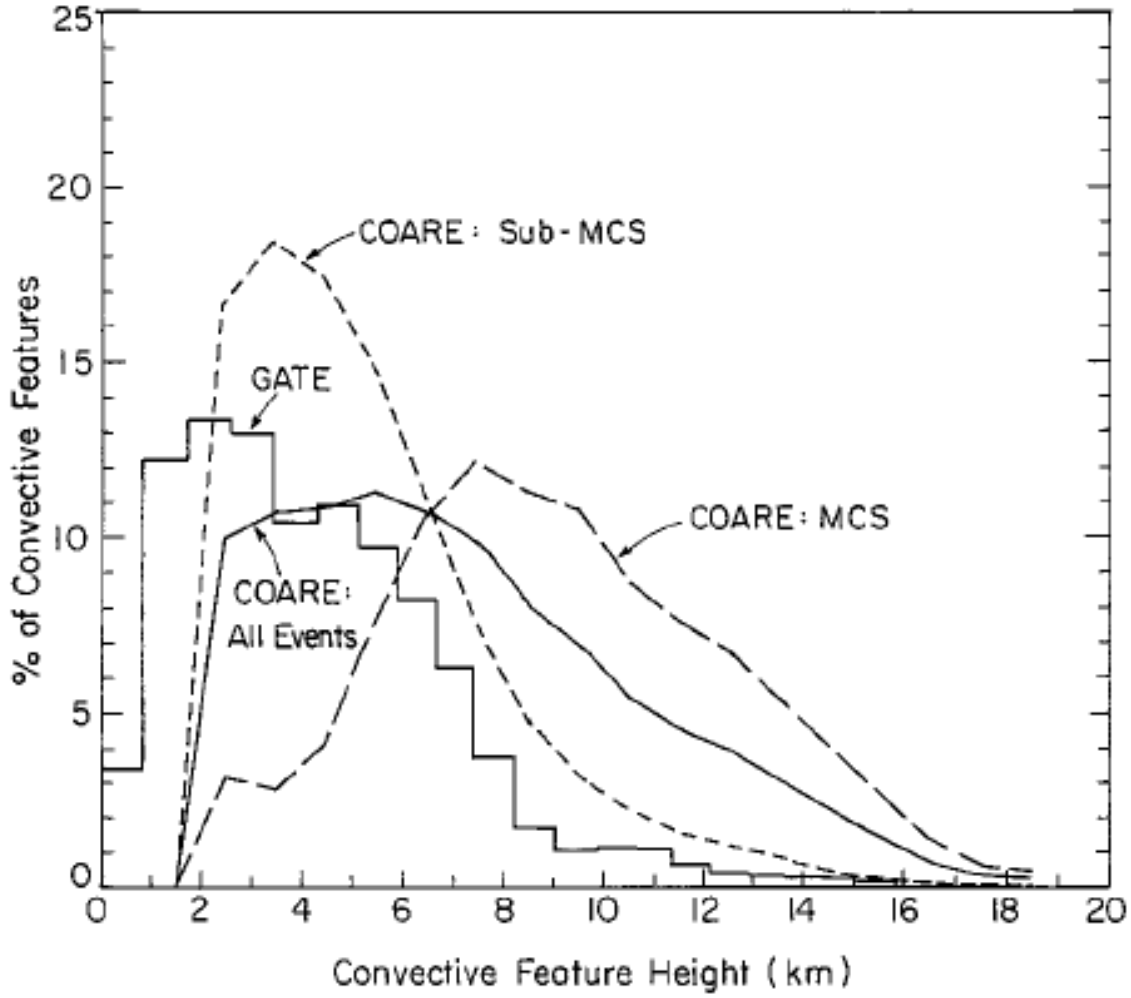

Figure 5. Frequency distribution of radar echo heights from GATE and COARE. See Johnson et al. [1999] for more details.

of these are often capped by the trade inversion, which ranges from 500 m to 2 km in height [Riehl 1954].

The solid line in Figure 4 marks the relative frequency of cloud-top height for active convection, in terms of individual convective features. The dashed curve factors in the size of each cloud to give an idea of relative areal coverage by cloud height. For the solid curve, a small convective cloud is treated the same as a large deep

cumulonimbus cloud (i.e., each is considered one convective feature); for the dashed curve, individual CloudSat fields-of-view (FOV) are considered. It is clear from the solid curve that, in terms of individual convective cells, shallow clouds of around 4 km in height dominate. A weaker peak is noted around 14 km, but this peak becomes dominant in the dashed curve. This shows that, although there are fewer deep cumulonimbus clouds than shallow clouds, these take up a larger horizontal area.

In contradiction to other studies looking at cloud distributions [Casey et al. 2007], the profile does not show a clear three-peak distribution. That being said, the solid curve resembles the sub-mesoscale convective system (MCS) curve in Figure 5, taken from Johnson et al. [1999], with a peak in convective feature distribution around 3 km, followed by an exponential decrease. In their conclusion, Johnson et al. [1999] noted that, in terms of convective features, shallow cumulus were the most frequent cloud type, with congestus being fewer and deep clouds rare. They also noted that deep clouds provided 90% of the rainfall for the tropics, compared to 9% for congestus clouds and 1% for cumulus clouds. Therefore, the trimodal distribution is meant to represent three distinct cloud types that may not necessarily be seen using the same metric (be it height, rainfall, etc.).

Finally, though the Luo et al. [2008] method used above is designed to identify optically-thick convective cloud, the erroneous inclusion of areas of stratiform precipitation cannot be ruled out. Of the coincident scans between CloudSat and the Tropical Rainfall Measuring Mission (TRMM) Precipitation Radar (PR) during January 2007, available through the 2D-CLOUDSAT-TRMM data product, only two scans

included optically-thick clouds, as identified through our method, and neither was associated with precipitation at the time of the TRMM overpass. Expansion of this study into longer time periods should allow for a better assessment of this issue.

CHAPTER III

DETERMINATION OF FINAL CLOUD-TOP HEIGHT

One problem with polar-orbiting satellites, including CloudSat and CALIPSO, is that they provide periodic observations of the atmosphere, with the time between the observations being much greater than the time scale of the lifecycle of a convective event. As a result, there is no expectation that a cloud observed by an A-Train satellite is at its maximum altitude. Luo et al. [2009] categorized observations of mid-level clouds as *transient congestus*, or those convective clouds that are observed at mid-levels when CloudSat passes over, but are in the process of rising to become deep cumulonimbus clouds; and *terminal congestus*, or observed congestus convection that remains at mid-level heights. To do so, they compared cloud-top temperatures (CTT) from the MODIS instrument onboard the Aqua satellite with environmental temperatures from ECMWF analysis, assuming a 6 K difference between calculated MODIS CTT and actual top of the cloud due to instrumental limitations. A simple 1 K sensitivity test, however, altered the final statistics regarding what constitutes transient congestus by 81% (31% versus 56%).

In this study, I differentiate these two categories using data from the National Centers for Environmental Prediction/Aviation Weather Center (NCEP/AWS) Infrared Global Geostationary Composite. This combines data from the GMS (Japan), GOES-East, GOES-West (USA), and Meteosat (Europe) geostationary satellites into half-

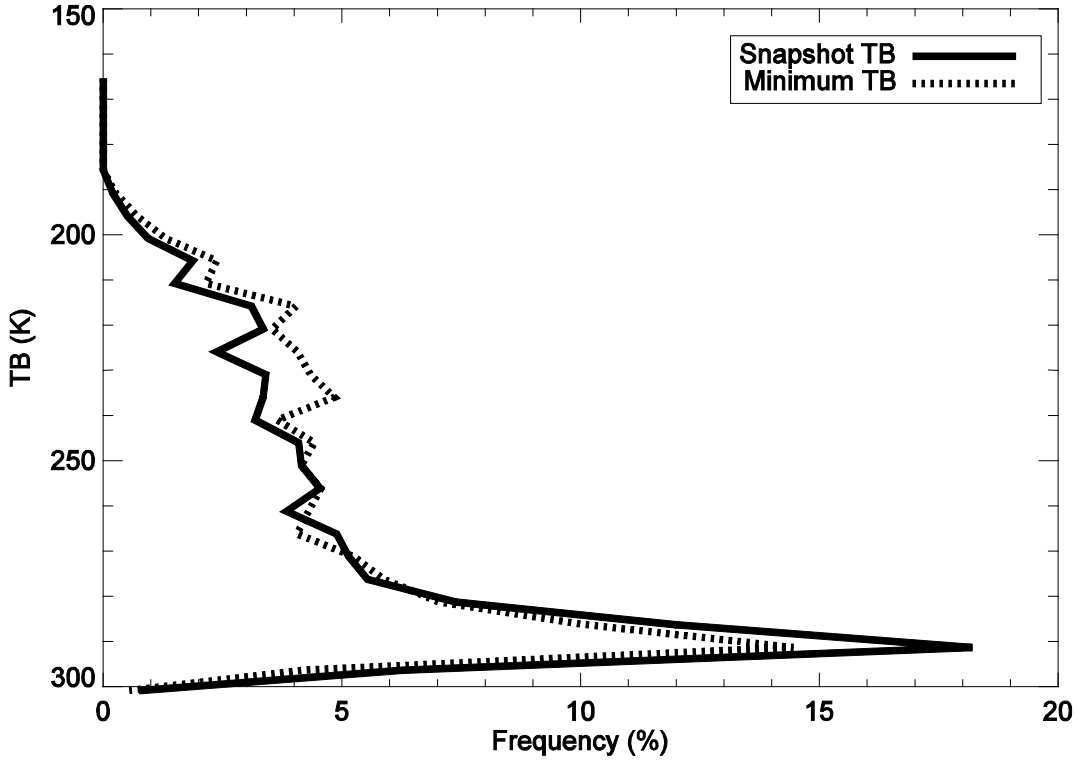

Figure 6. Frequency of minimum brightness temperatures (Tb) for cloud events, binned into 5K bins. Solid line marks the distribution of minimum Tb at the time of the A-Train overpass, and dashed line the distribution of minimum Tb over the entire lifecycle of the cloud events seen by the A-Train satellites. The sum of each data point in each curve adds to unity.

hourly composite images with 14 km × 14 km resolution. Nearly all the tropics are covered by this product, with the exception of a gap around 70°E longitude.

For the NCEP/AWS analysis, a box is centered on the cloud feature, with sides of length 0.25°. All NCEP/AWS pixels within this box are analyzed to obtain the minimum brightness temperature in this box. Then, for each half-hour composite file after the A-Train observation, the minimum brightness temperature in the box is again determined. If this temperature is lower than the previous minimum, the cloud is

considered to have risen in height. If the minimum temperature in the region is higher than the previous minimum, the cloud is assumed to be dissipating. The overall minimum brightness temperature for the cloud feature is then recorded as the lowest minimum brightness temperature. Admittedly, this method is unable to see changes in cloud height on time scales less than 30 minutes; in the case of short-lived convection, the cloud could rise and fall within that time frame. Nevertheless, I believe that this provides a better method for tracking the life cycle of clouds on a tropics-wide scale.

Figure 6 shows the relative frequency distributions for the minimum T_B at the time of the A-Train overpass (snapshot T_B, solid) and the minimum T_B over the entire lifecycle of the cloud (dashed). As in Figure 4, more clouds are noted near the surface, with a mode in both distributions near 290 K. However, the lifecycle minimum T_B curve shows fewer T_B measurements near the surface and more higher in the atmosphere. It should be noted that the snapshot T_B curve does not perfectly match the convective feature distribution in Figure 4; this is most likely due to the differences in FOV between CloudSat and NCEP/AWS, with beam-filling effects yielding T_B values that do not correlate with the actual CloudSat cloud-top height.

To differentiate between convective cloud types, we combine the feature height and minimum T_B distributions from Figures 4 and 6, respectively. Table 1 separates the observed convective features for January-February 2007 into nine categories based on CloudSat cloud-top heights and geostationary satellite minimum brightness temperatures. Of the 1308 clouds identified by CloudSat as congestus, 29.6%

Table 1. Number of observed clouds by CloudSat height and NCEP/AWS minimum brightness temperature over the life cycle of the cloud, along with the categories these clouds are assigned.

	Cloud height < 5 km	5 km ≤ cloud height ≤ 9 km	Cloud height > 9 km
Min T_B > 273K	736 (shallow)	505 (congestus)	251 (deep)
243 K≤ Min T_B ≤ 273 K	290 (congestus)	416 (congestus)	283 (deep)
Min T_B < 243K	220 (deep)	387 (deep)	523 (deep)

(387/1308) are transient, rising to become deep clouds. This is lower than the 44% found by Luo et al. [2009], but close to their 31-56% margin of error. Seemingly erroneous answers, such as a high final T_B corresponding to a cloud height greater than 9 km, are most likely due to the beam-filling issue described above.

Also included in this table is the categorization for which these particular clouds will be included for the rest of this paper. Clouds that are either associated with cloud-top heights greater than 9 km or minimum T_B less than 243 K will be considered a "deep" cloud. Remaining clouds with either a cloud-top height between 5 and 9 km or a minimum T_B between 243 and 273 K will be considered a "congestus" cloud. All other clouds, which have a cloud-top height below 5 km and a minimum T_B greater than 273 K, will be considered a "shallow" cloud. Altogether, this analysis will look at measurements in the presence of 736 shallow clouds, 1211 congestus clouds, and 1664 deep clouds.

CHAPTER IV

ENVIRONMENTAL PARAMETERS DATA

A) Atmospheric InfraRed Sounder (AIRS)

Collocated with the CloudSat cloud retrievals are temperature and relative humidity observations from the AIRS instrument onboard the *Aqua* satellite [Fetzer et al. 2005]. The core of this instrument is a high-resolution infrared sounder measuring in 2378 spectral channels between 3.74 and 15.4 μm. AIRS retrievals have an effective resolution of ~50 km in the horizontal, with an accuracy of ~10% for an individual measurement.

The standard product (AIRX2RET) is more commonly used to look at temperature and water vapor in the atmosphere. However, its vertical resolution is too sparse (100 hPa between bins) to produce reliable temperature lapse rate information. Instead, we utilize the level-2 support product (AIRX2SUP), in which temperature and water vapor are retrieved with about 20 hPa resolution in the vertical (the intrinsic resolution of the measurement is the same as for the standard product: 1 km in the vertical for temperature and 2 km in the vertical for water vapor). One quantity used in the calculation of relative humidity, the saturated specific humidity, is included in the AIRS standard product, but not the support product. We therefore calculate this quantity using the temperature at a given height and the Goff-Gratch function. Figure 7 shows a sample collocated scan between AIRS and CloudSat; black marks areas of cloud identified by CloudSat, and shading marks AIRS-retrieved temperatures.

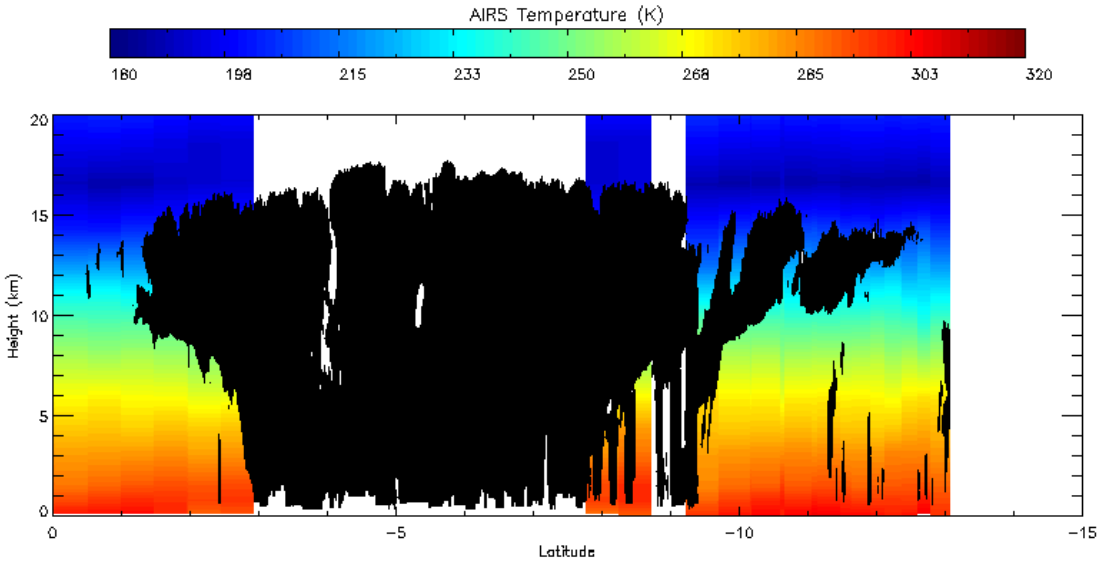

Figure 7. Sample collocated scan between AIRS and CloudSat, from July 1st, 2006.

AIRS level-2 products are computed using a cloud-clearing algorithm that can yield atmospheric constituent amounts in fields-of-view with as much as 90% cloud cover. However, this doesn't mean that we can trust all data values given in the product, so I will only use data that passes the "best" test. That is, either the quality flag for water vapor is set to 0, or it is set to 1, in which case we only use water vapor and temperature values for heights above the PBest quality flag (above this height, the RH data is considered high quality). This means that more data points will be utilized for a mean temperature and/or relative humidity profile in the upper atmosphere than closer to the surface. In addition, while shallow and congestus clouds are typically small in diameter (~3-5 km), deep cumulonimbus clouds are more likely to be associated with large stratiform and anvil regions that may fill up the field of view (FOV), rendering water vapor and temperature profiles directly over the cloud unusable. As we are interested in the environmental conditions in which different cloud types form, we look at a 5×5 FOV

range centered on the coincident value, yielding an effective resolution of 250 × 250 km. We then calculate the average temperature and RH measured by these FOVs at each pressure level, revealing the environmental temperature and RH in the vicinity of the convective feature. Three-level averages of each variable are then plotted. This averaging is done to reduce noise in the level-by-level curve.

B) ERA Interim Reanalysis

As mentioned in Chapter III, polar-orbiting satellites such as *Aqua* provide only snapshot measurements (at most) twice a day over a specific location. To see how the large-scale temperature and RH evolves over the lifecycle of a convective cloud, we utilize data from the ECWMF ERA-Interim Re-Analysis [European Center for Medium-Range Weather Forecasts, 2009]. This reanalysis product assimilates a variety of different atmospheric instruments into a single product with 1.5°×1.5° spatial resolution every 6 hours. The nearest ERA pixel is identified for each convective cloud observation. Temperature and RH values are then identified 24 hours prior to and after the time of the CloudSat overpass. It should be noted that some issues remain regarding the reliability of reanalysis RH measurements, particularly over the open ocean [Daoud et al. 2009]. For this reason, the results discussed here should only be considered in comparison with the AIRS observations.

CHAPTER V

RELATIVE HUMIDITY AND CONGESTUS CLOUDS

Based on the dry-air layer theory of congestus cloud-height limitation, one would expect to find lower mid-tropospheric RH in the presence of congestus clouds than in the presence of deep clouds. Using the method described in Chapter III and the data of Chapter IV, the evidence for such a relation between RH and cloud-top height is assessed below.

Figure 8 shows the mean RH profiles as viewed by AIRS in the presence of shallow, congestus, and deep clouds. The error bars represent the observed value ±2 times the sampling error

$$S_E = \frac{\sigma}{\sqrt{N}}$$

Thus, the error bars represent the 95% confidence interval of the mean RH values at a given height.

Free-tropospheric RH is lowest in the presence of shallow clouds, with a mean RH of approximately 40% from 750 to 350 hPa. This value is statistically significant throughout this depth. As shallow clouds are associated with warm and low cloud-top heights, much of the free troposphere is unaffected by the convection. Congestus mid-tropospheric RH values are higher than those observed in the presence of shallow clouds by about 15%, but are lower than the RH values observed in the vicinity of deep convective clouds by about 5%. The congestus and deep mean values are significant within a 95% confidence interval test (as shown by the error bars) between 600 and 300

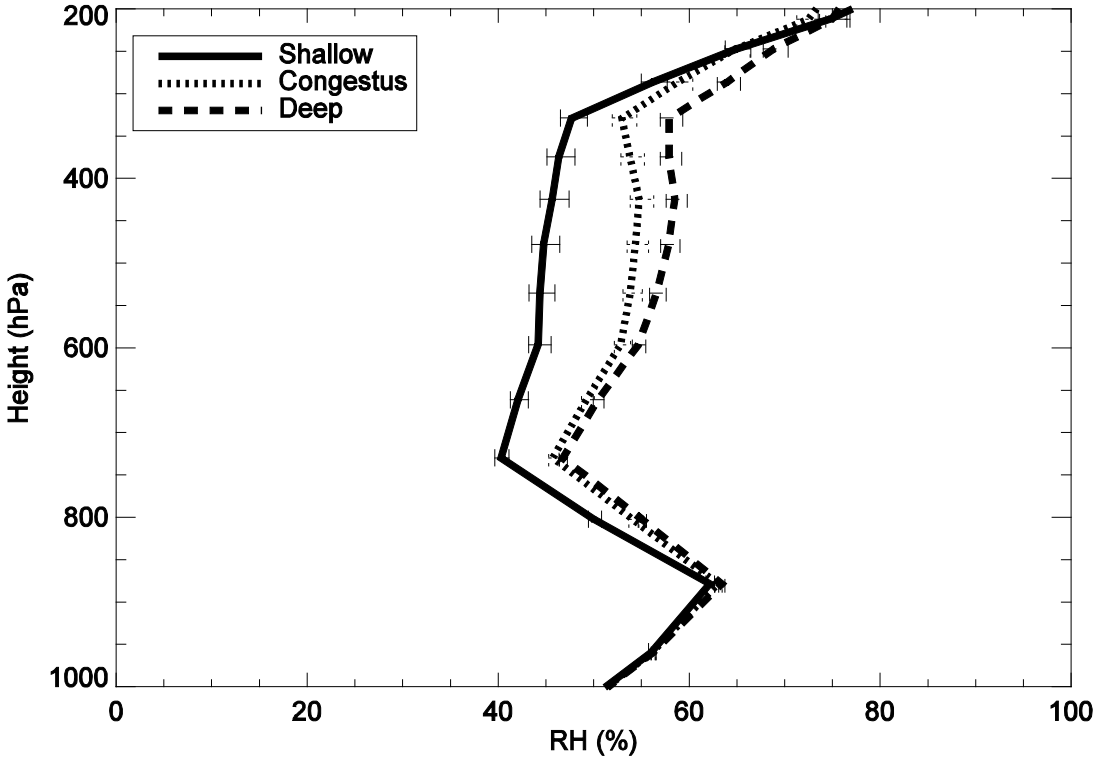

Figure 8. Mean RH profile in the presence of shallow, congestus, and deep clouds. Error bars mark the observed value ±2 times the sampling error.

hPa. Comparing only the terminal and transient congestus categories defined by Luo et al. [2009], as described above, the mean RH profile is virtually identical below 500 hPa (Figure 9), but the terminal congestus curve is drier above this level. This shows the importance of separating terminal from transient congestus.

To further investigate this difference, Contoured Frequency by Altitude Diagrams (CFADs; Yuter and Houze [1995]) relating frequency of occurrence of RH values at a given height were calculated for each cloud type. Figure 10 shows the difference between the RH CFADs for congestus and deep clouds. Grey areas indicate RH values at a given height where congestus clouds are more frequently observed than

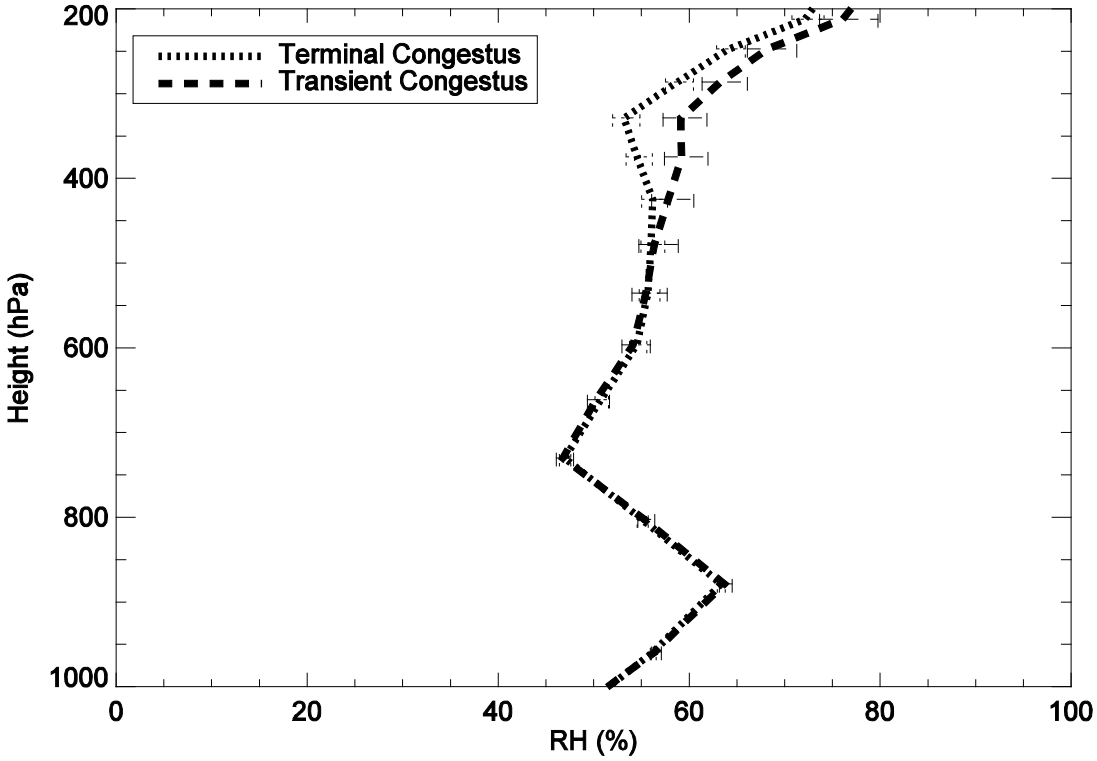

Figure 9. Mean RH profile in the presence of terminal congestus (marked as the dotted "congestus" line) and transient congestus (marked as the dashed "deep" line), as defined by Luo et al. [2009].

deep clouds; white closed-in areas mark areas where deep clouds are more prominent. Through a deep layer of the atmosphere between 800 and 250 hPa, congestus clouds are more frequent than deep clouds when the relative humidity is below ~30%. According to the dry-air capping theory of congestus cloud-top heights, anomalously dry air in this part of the atmosphere should lead to a greater prominence of congestus clouds. Figure 10 confirms this hypothesis by first identifying the congestus and deep clouds, then separately looking at the associated RH values.

Figure 11 shows the difference in RH for shallow (solid) and deep (dashed) clouds compared to congestus RH, at (a) 24 hours prior to convection, (b) near the time

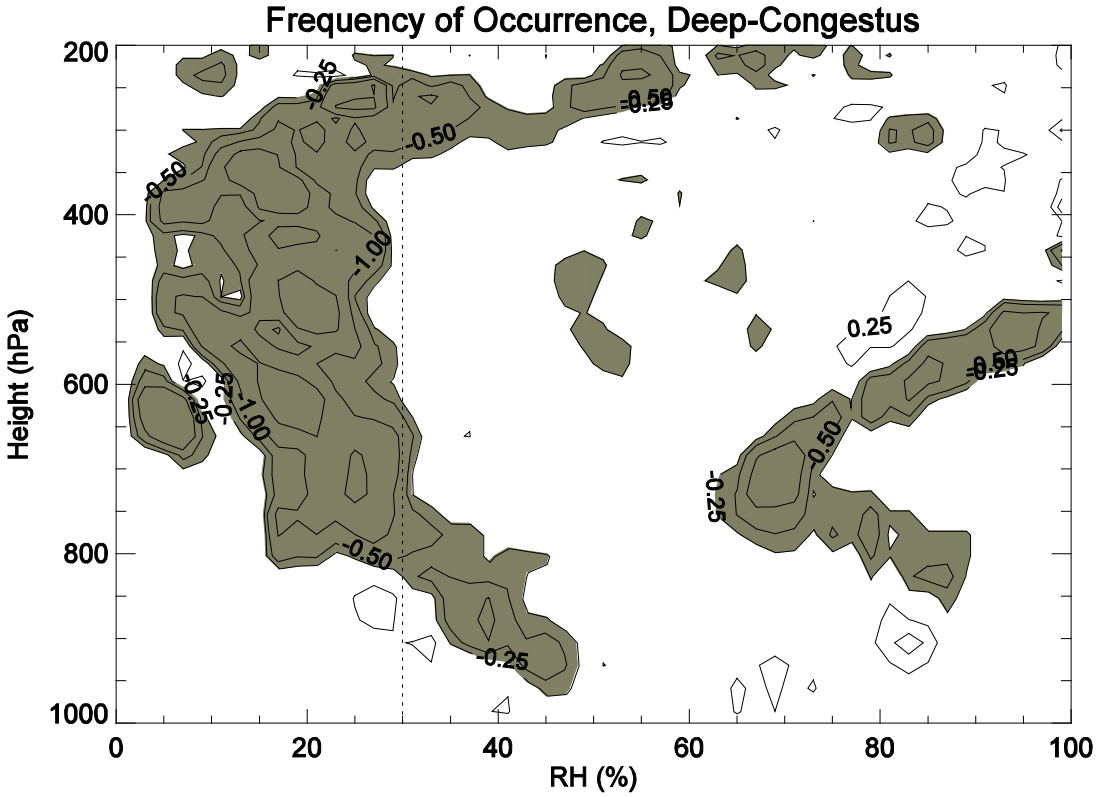

Figure 10. Contoured Frequency by Altitude Diagram (CFAD) of the differences between RH observations between mid-level congestus and deep cloud observations. Gray shading indicates where RH values are more frequent in the presence of congestus clouds; clear shading where RH values are more frequent in the presence of deep convection. A value of -2 signifies a drop in occurrence of 2% from congestus to deep clouds.

of convection, and (c) 24 hours after convection based on ERA data. Positive values for the solid curve signify where RH in the presence of congestus is higher than in the shallow case. Large increases in free-tropospheric RH are noted 24 hours prior and after convection. The dashed curve in Fig. 11b shows that RH is higher in the presence of congestus clouds than shallow clouds in the mid- to upper-troposphere, and higher in the presence of deep clouds than congestus clouds throughout the atmospheric column. The

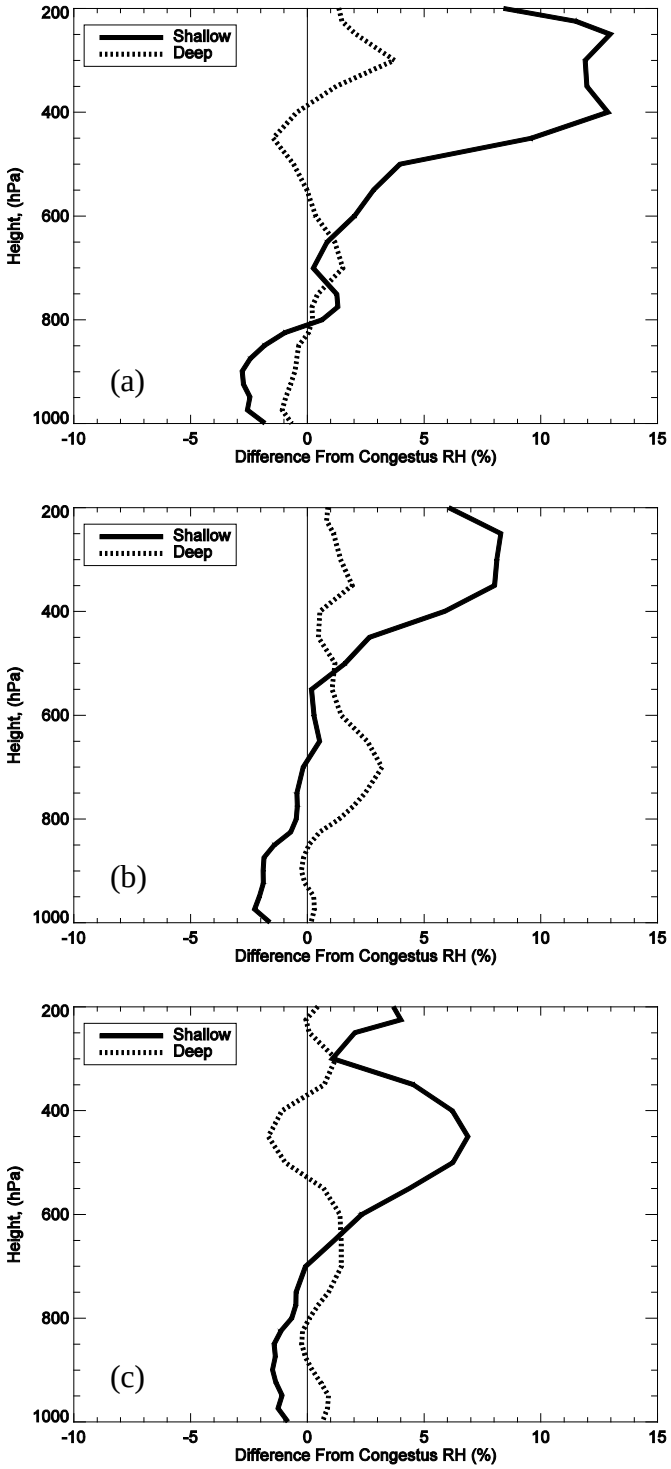

Figure 11. Difference in RH; solid curve shows congestus-shallow RH, and dashed curve shows deep-congestus RH; at (a) 24 hours prior to convection, (b) time of convection, and (c) 24 hours after convection.

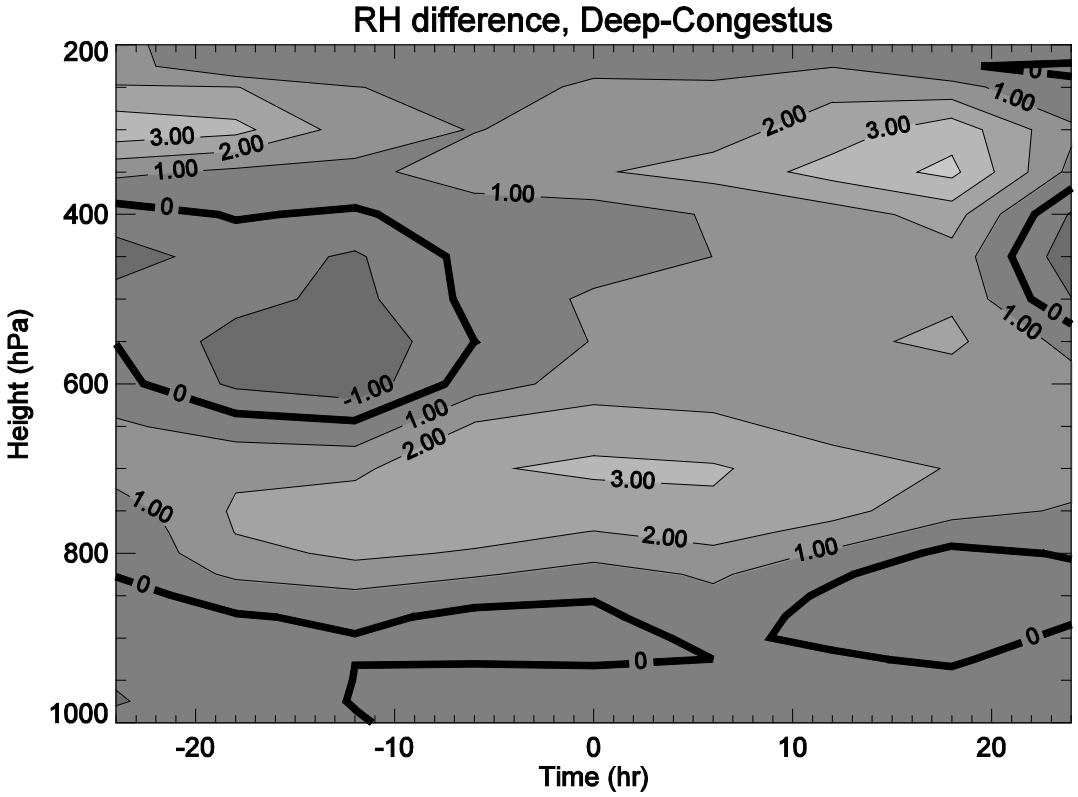

Figure 12. The difference between deep and congestus RH for the 48-hour period; positive values (light) indicate where RH is higher in the presence of deep clouds, and negative values (dark) where RH is lower.

profile 24 hours prior, however, suggests that RH is lower before congestus cloud formation at 450 hPa.

Figure 12 shows the difference between the congestus and deep case for the full 48-hour period. Higher RH values are noted in between 800 and 600 hPa in the presence of deep clouds. Before the convective feature, RH is slightly lower in the presence of deep clouds between 600 and 400 hPa, for reasons that are unclear. After convection, higher deep RH values are noted between 600 and 400 hPa. This suggests that deep convection is moistening the upper troposphere on scales discernable by ERA.

While Figure 12 suggests a large difference in RH between 800 and 600 hPa separating congestus and deep clouds, Figure 8 shows little to no difference at these levels. Instead, Figure 8 notes a larger difference between 600 and 300 hPa. The cause of this discrepancy between the AIRS and ERA data is unknown, but both figures nevertheless show an increase in free-tropospheric RH in the environment surrounding deep cloud observations than for congestus clouds.

CHAPTER VI

TEMPERATURE LAPSE RATE AND CONGESTUS CLOUDS

Based on the stable-layer theory of congestus cloud-height limitation, one would expect to find lower changes in temperature with respect to pressure (dT/dp), and therefore greater stability, in the presence of congestus clouds than in the presence of deep clouds. Using the method described in Chapter III and the data of Chapter IV, the evidence for such a relation between lapse rate and cloud-top height is assessed below.

Figure 13 shows the differences in lapse rate between the three convective cloud categories. The wide error bars in the lower troposphere are a by-product of the fewer observations used at these heights (as explained in Section IV) as well as the greater variability in temperature lapse rates nearer the surface (as results from surface heating/cooling). High lapse rates signify unstable environments; thus, the lower the value on this graph, the more stable the atmospheric profile is.

In the midtroposphere, shallow clouds are associated with slightly more unstable environments than for the other two cloud categories. This is to be expected; shallow clouds are often blocked from further development by a trade inversion, the result of subsiding air [Simpson 1992]. (The trade inversion is not evident in the shallow curve of Figure 13, but this is most likely due to averaging effects, as well as potential issues in AIRS retrievals near the surface.) This subsidence leads to an atmospheric profile that more closely resembles a dry adiabatic lapse rate than a stable atmospheric lapse rate.

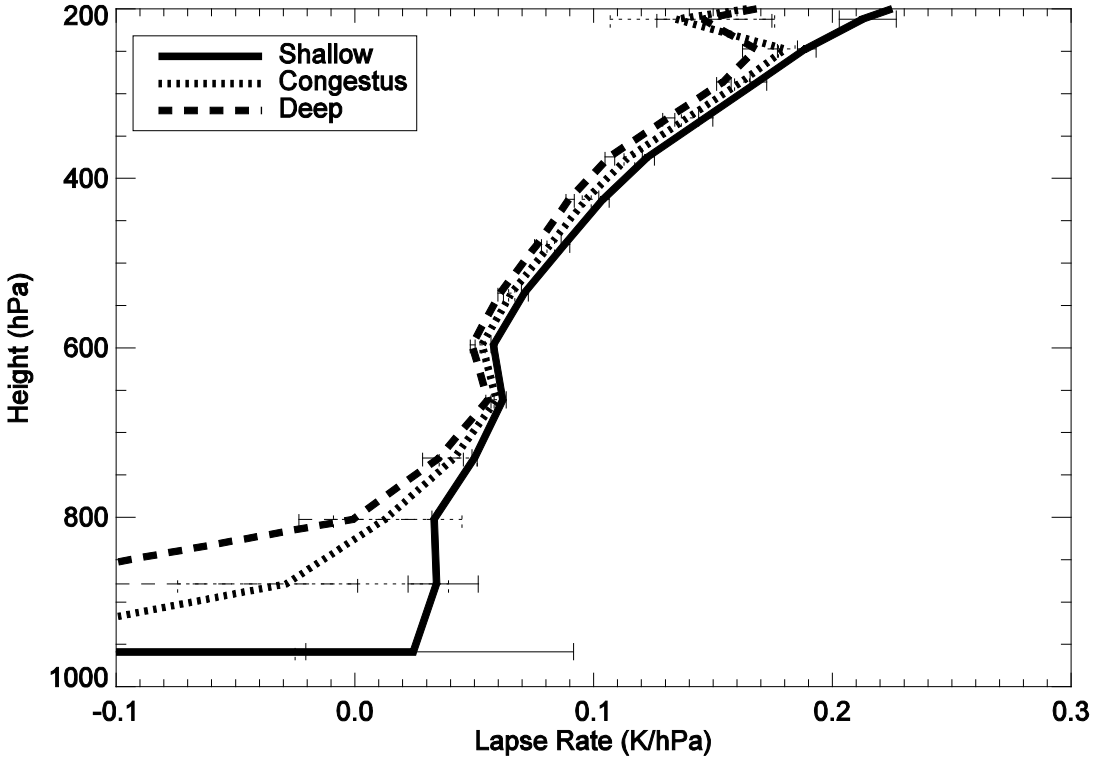

Figure 13. Mean temperature lapse rate profile in the presence of shallow, congestus, and deep clouds. Error bars mark the observed value ±2 times the sampling error.

Throughout the midtroposphere, the lapse rate curve for congestus clouds appears to be slightly more unstable than the curve for deep clouds. Two things are apparent in comparison to Figure 8. First, given the large difference in mean RH profiles between these two categories, the similarity in the lapse rate profiles is striking. At no level is the difference between the lapse rates statistically significant. Second, ignoring the error bars and simply looking at the mean lapse rate values plotted, a more stable atmosphere in the presence of deep clouds would be in contradiction to the mechanisms expected from the stable layer theory of congestus cloud limitation.

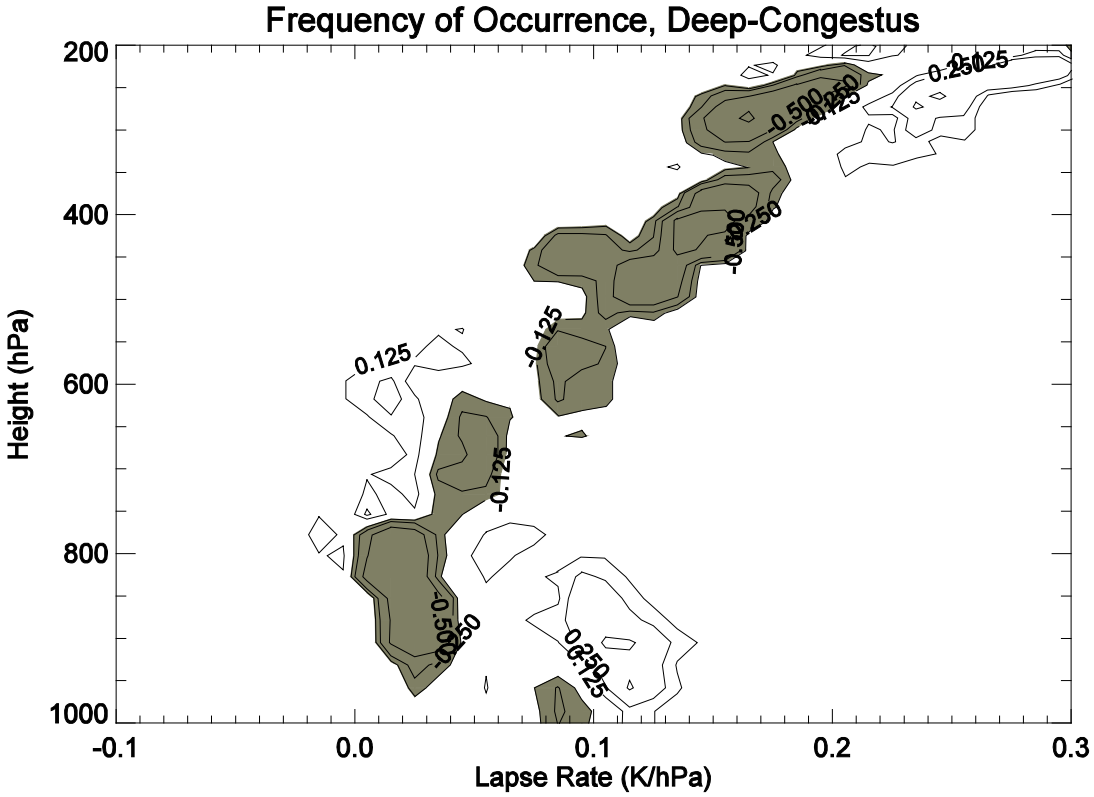

Figure 14. CFAD of the differences between lapse rate observations between mid-level congestus and deep cloud observations. Gray shading indicates where particular lapse rate values are more frequent in the presence of congestus clouds; clear shading where particular lapse rate values are more frequent in the presence of deep convection. A value of -0.5 signifies a drop in occurrence of 0.5% from congestus to deep clouds.

Figure 14 shows the difference between the CFADs for congestus and deep clouds. As with Figure 10, gray shading marks lapse rate values for which congestus is more frequent than deep clouds, and white shading where deep cumulonimbus is more prominent. The stability-capping theory says that congestus should occur more frequently when the midtropospheric lapse rate is small (i.e., stable). However, Figure 14 shows very slight differences in relative frequency between the cloud types, with "high" values only showing an increase or decrease in occurrence of 0.125%. In addition, the two contoured areas in Figure 14 near 600 hPa suggest that congestus is

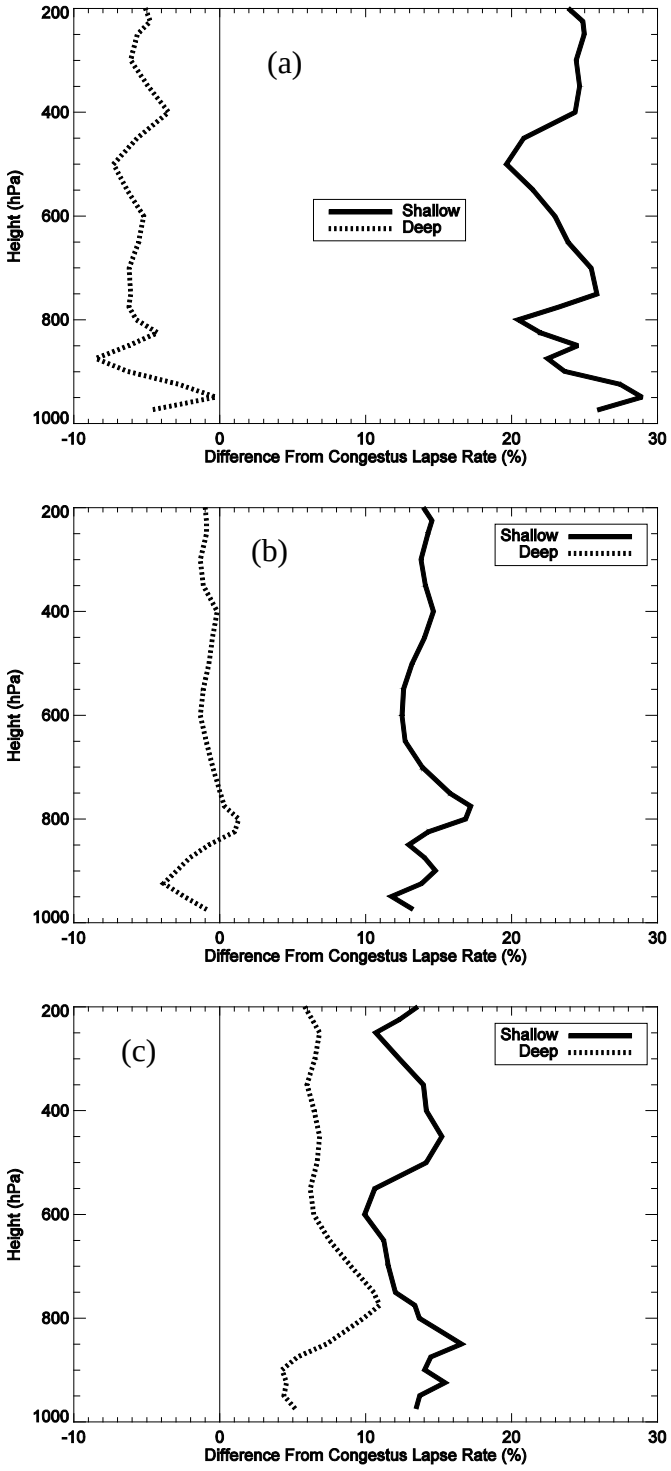

Figure 15. Difference in lapse rate for shallow (solid) and deep (dashed) clouds compared to congestus, at (a) 24 hours prior to convection, (b) time of convection, and (c) 24 hours after convection.

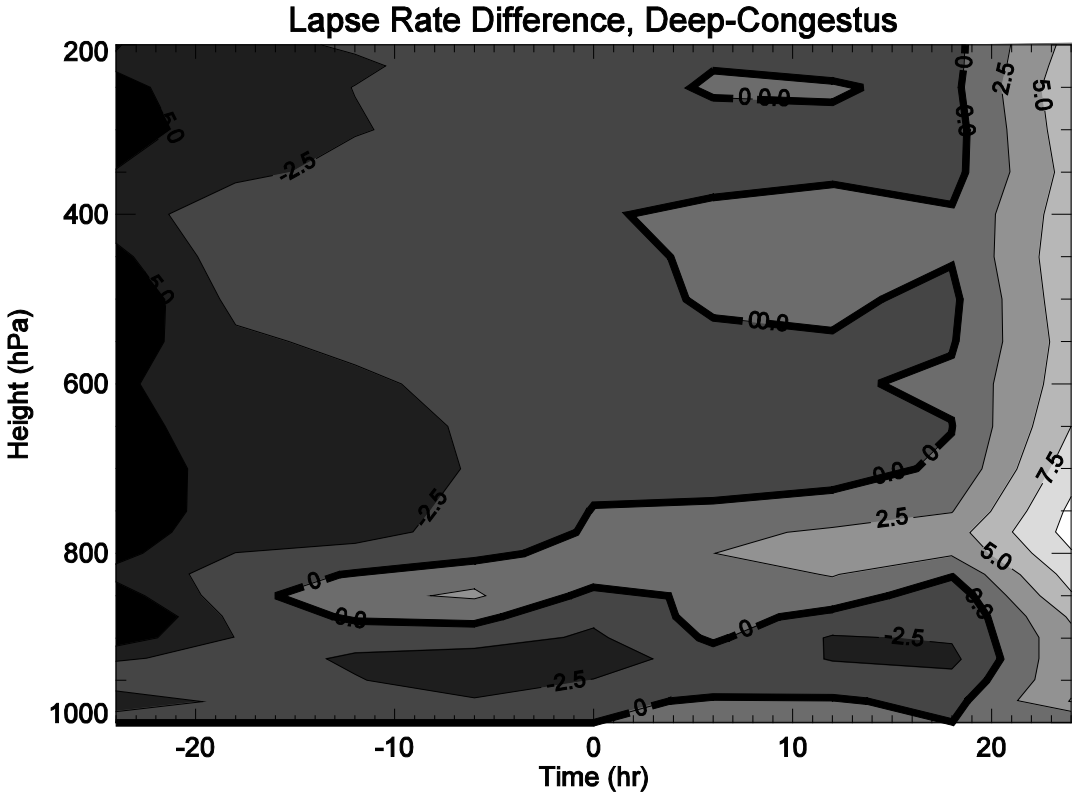

Figure 16. The difference between deep and congestus lapse for the 48-hour period; positive values (light) indicate where lapse rate is higher in the presence of deep clouds (i.e., a more unstable atmosphere), and negative values (dark) where lapse rate is lower.

more frequent when higher lapse rates are observed, and that deep clouds are more often associated with smaller lapse rates.

Figure 15 shows the ERA-calculated lapse rates for the 48 hours surrounding the cloud observations, separated by cloud type, and Figure 16 shows the difference between the lapse rate values for deep and congestus clouds. Twenty-four hours prior to convection, the atmosphere appears to be much more stable in the presence of congestus clouds than shallow clouds, as expected (see above). The atmosphere also appears to be 7% more stable for deep clouds than for congestus clouds, which again is contrary to the stable layer theory. Figure 15b, however, shows little difference between the lapse rates

for congestus and deep clouds. Figure 15c suggests that, 24 hours after congestus convection, the atmosphere is much more stable than the associated shallow and deep convection locations. The stable-layer theory suggests that the atmosphere before and during congestus convection is more stable than for deep convection, but says nothing about how the atmosphere should behave after convection.

Light colors in Figure 16 mark where the lapse rate is higher (i.e., more unstable) in the presence of deep clouds, and dark colors where the lapse rate is higher near congestus clouds. In the 24 hours before the cloud forms, the atmosphere is slightly more unstable where congestus clouds develop, and that in the 24 hours afterward, the atmosphere is more unstable where deep clouds have formed. The latter may be related to the gregarious nature of tropical convection [Mapes 1993] whereby conditions near an existing mesoscale convective system (MCS) are more favorable for the development of additional convection. Again, however, the absence of increased stability in the environment in which congestus clouds form is striking.

CHAPTER VII

ASSESSMENT OF CAPPING MECHANISMS

The AIRS mean lapse rate profiles in Figure 13 could, in effect, be considered an inconclusive result concerning the role of stable layers in congestus occurrence. If assuming a null hypothesis of lapse rate (congestus) = lapse rate (deep), there is not enough information to prove this hypothesis to be incorrect. The statistical distribution of AIRS observations in Figure 14 suggest some slight differences between the two cloud types, but these suggest a relation that goes against the lapse-rate capping theory of congestus cloud formation. The ERA profile in Figure 15b shows virtually no difference in the lapse rate profiles between congestus and deep clouds. These three figures together raise questions as to the viability of the stable-layer theory.

On the other hand, the dry-air capping theory is lent support by the satellite and reanalysis data. Clear differences in midtropospheric RH are noted between congestus and deep clouds, both in terms of direct measurements by the AIRS instrument onboard *Aqua* as well as the ERA Interim Reanalysis product. A threshold of 30% RH could also be identified in the midtroposphere, below which congestus clouds are more likely to be observed than deep clouds.

That being said, this does not definitively answer the question of which comes first: deeper clouds or higher free-tropospheric moisture. If the moist mid-troposphere is advected in, then the absence of congestus can be attributed to the large-scale motion. If

the atmosphere is moistened by congestus, allowing deeper clouds to form, then this can instead be attributed to smaller-scale effects.

Finding the answers to this question has repeatedly been hampered by the limitations of observational evidence. Despite the vast improvements in horizontal and vertical scale and quality/frequency of data, satellite observations nevertheless run into the issue of limits in temporal scale. Polar-orbiting satellites are necessary to observe the small (often < 5 km) convective features present, but because of the nature of the polar orbit, they cannot view the life cycle of the cloud. Geostationary satellites can fill in some of the gaps with respect to cloud-top brightness temperatures, but any potential temperature and water vapor profiles would have much coarser resolution (~14 km with most geostationary products today), missing many of the shallow cumulus and mid-level congestus features.

To definitively answer the question of which came first, the deeper clouds or the moist free troposphere, would require atmospheric soundings before and after the convective feature has grown and dissipated. Even if radiosondes and ground-based sounders are available to take these measurements for the same cloud, potential cloud movement would further complicate observational measurements.

Given these difficulties, models may pose the best (if not only) method for definitively answering this question. Zuidema et al. [2006] utilized a buoyancy-sorting model [Raymond and Blyth 1992] to answer this question, using data from the EPIC campaign. Their findings supported the lapse-rate capping theory, in disagreement with the results here. Figure 17 shows sample results using the mean T and RH profile from

TOGA-COARE [Ciesielski et al., 2003]. Panels a and b mark the lapse rate and RH, respectively. Panels c through e show the probability of cloud detrainment at a given height, assuming maximum liquid water mixing ratios of 1 kg/kg of condensed water, 3 kg/kg, and 5 kg/kg, respectively. Peaks near 950 mb, 500 mb, and 200 mb are noted on panels c-e. These line up well with the three modes of maximum cloud-top height suggested by the trimodal distribution theory.

Initial attempts to utilize AIRS data with this model (Figure 18) encountered problems resulting from issues with the boundary-layer AIRS RH measurements. Using the AIRS mean T and RH profiles, no convection rose above 900 hPa. Figure 19 shows results for a run using the AIRS T profile, but the TOGA-COARE RH profile (solid), along with the original TOGA-COARE run from Figure 17 (dashed). Though the distribution is less smooth, it is clear that deep convection can be induced using the AIRS T profile. Figure 20, on the other hand, uses the TOGA-COARE T profile and the AIRS RH profile (solid; dashed line again is the original TOGA-COARE run). As in Figure 18, convection once again does not rise above the boundary layer. The low surface-layer RH values measured by AIRS are most likely a result of surface multiple scattering, and its effects on the returned power values. As the surface layer is most important in initializing convection, this method cannot be utilized with the data as given. That being said, this should not be taken as an issue with the RH values from AIRS as a whole; AIRS still provides useful data in the free troposphere, the area in which this study is interested.

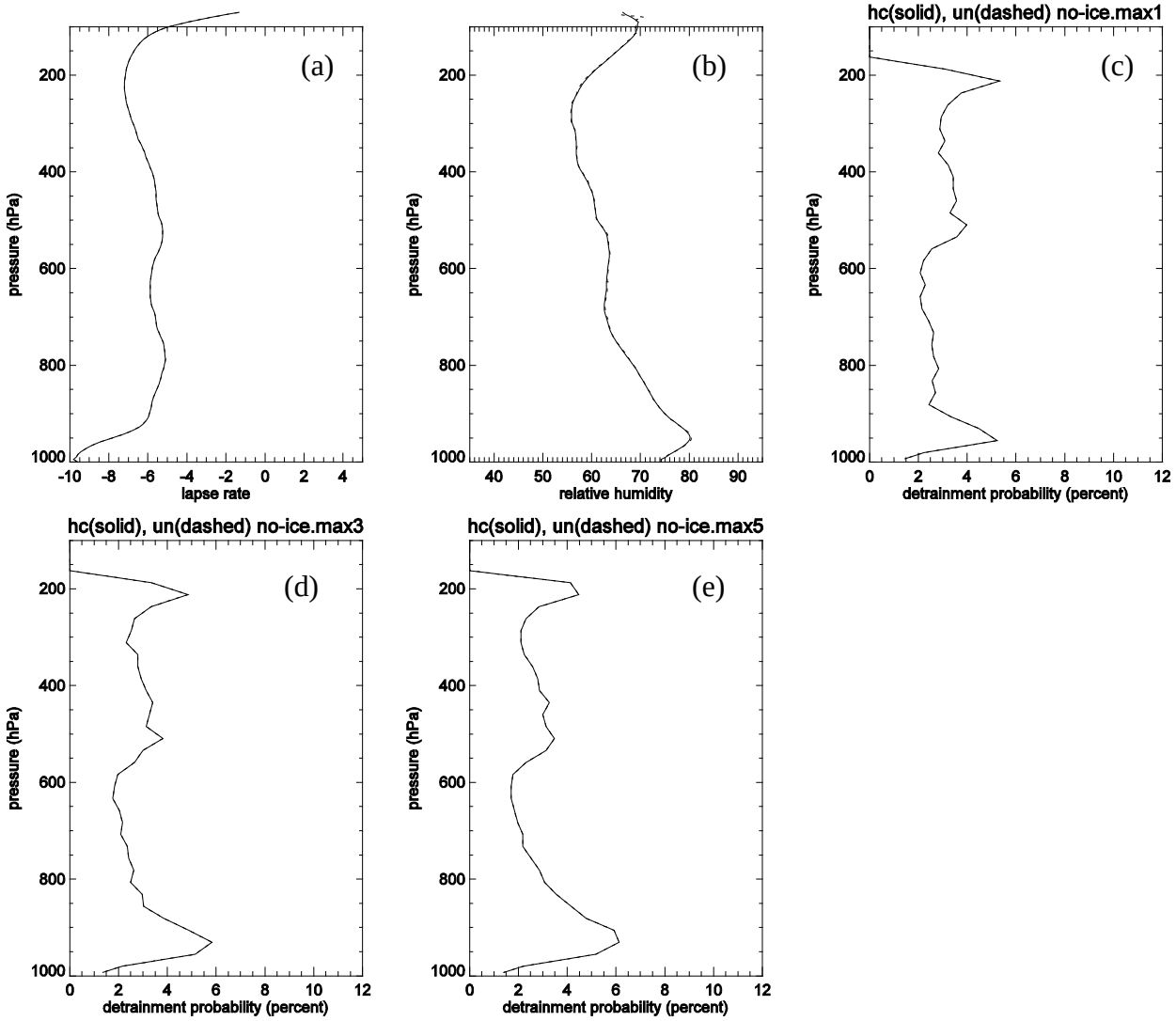

Figure 17. Results from using TOGA COARE mean T and RH profile in the Raymond-Blyth sorting model.

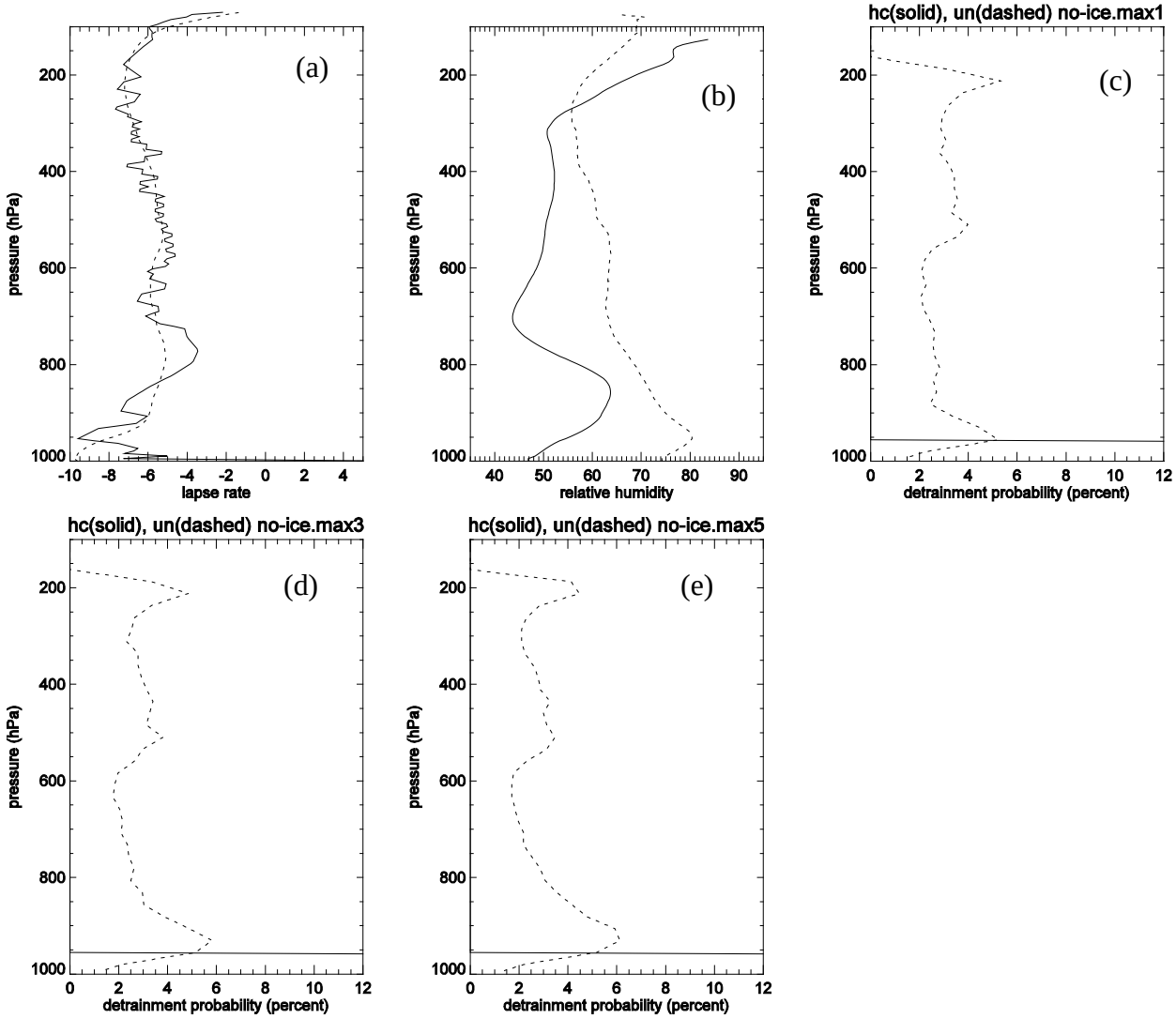

Figure 18. Results of using AIRS mean T and RH profiles in the Raymond-Blyth buoyancy sorting model.

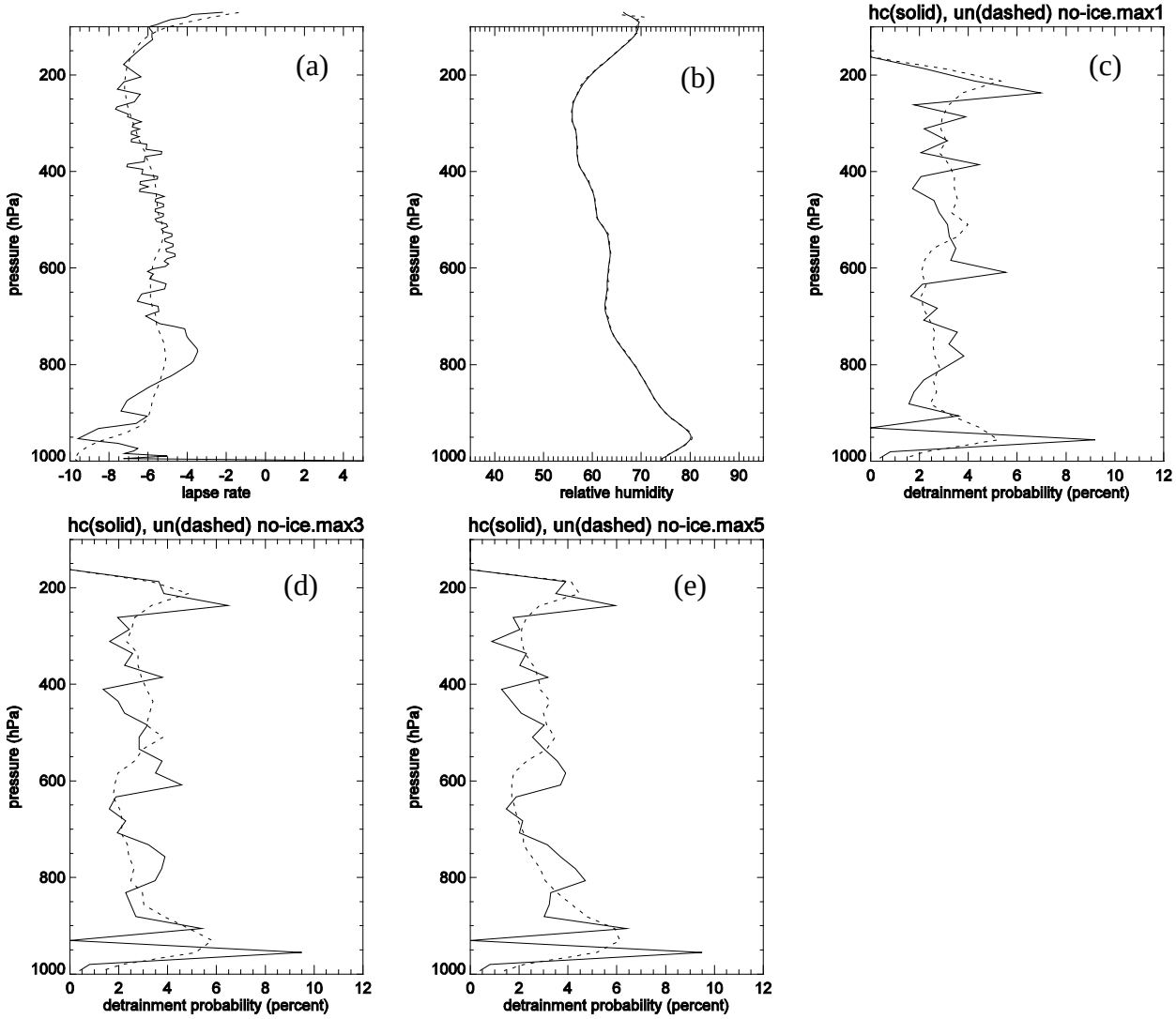

Figure 19. Results of using AIRS mean T and TOGA-COARE mean RH in the buoyancy-sorting model.

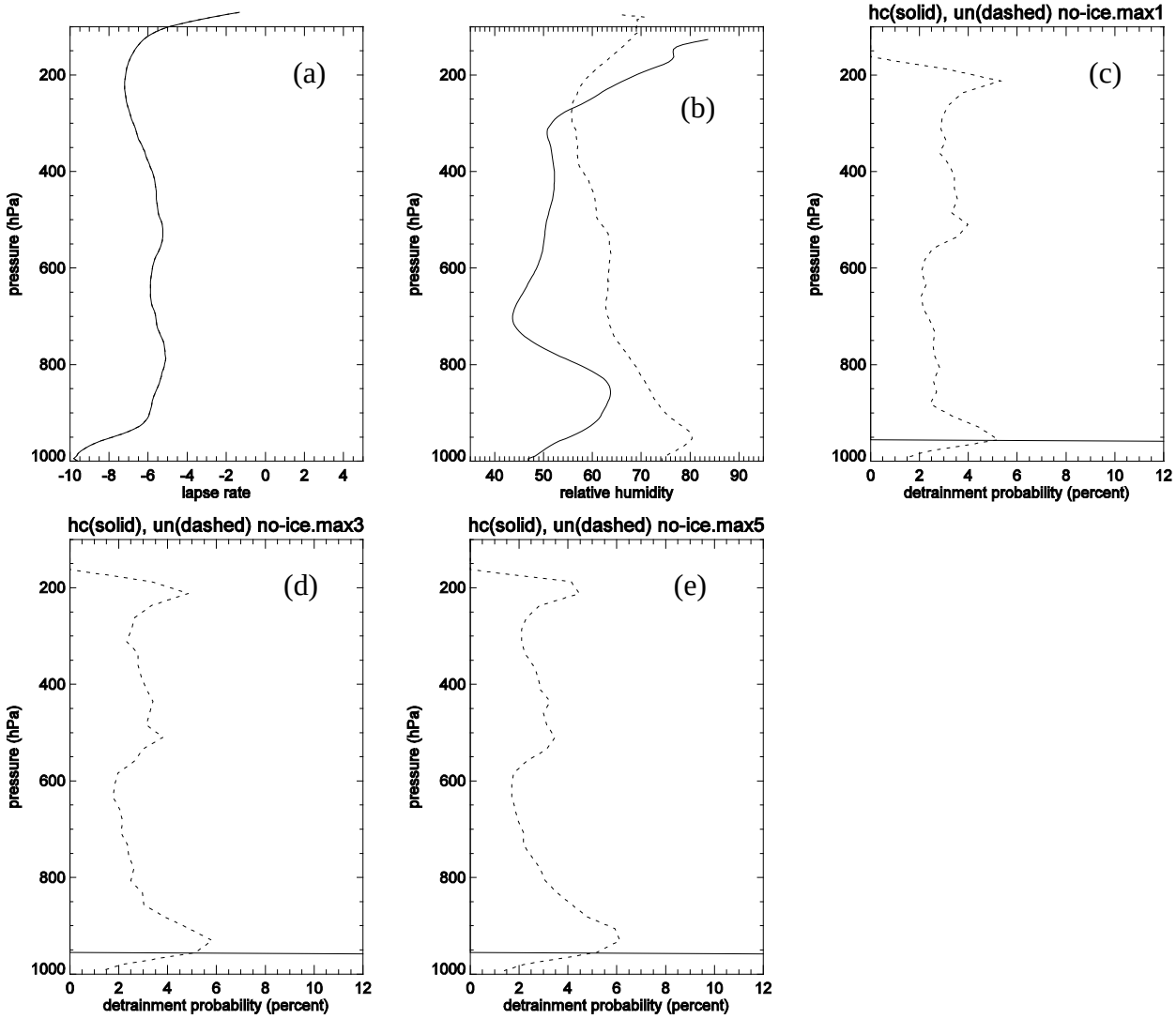

Figure 20. Results of using TOGA-COARE mean T and AIRS mean RH in the buoyancy-sorting model.

Recent studies using cloud-resolving models [Redelsperger et al. 2002; Jensen and Del Genio 2006; Kuang and Bretherton 2006; Khairoutdinov and Randall 2006] suggest that rising and detraining clouds moisten the atmosphere, which allows newer clouds to rise to higher heights, continuing the cycle until clouds reach the upper troposphere. While Figures 8-12 cannot definitively prove these modeled results correct, they do seem to support the results. Further study with both kinds of models, as well as identifying preferred sources of quality data, will help answer this important question of convective-cloud capping.

CHAPTER VIII

IDENTIFYING DRY AIR LAYERS*

Midtropospheric dry layers, in addition to potentially acting as a cap to congestus clouds, also have implications in global warming theory. Pierrehumbert [1995] noted the importance of dry "radiator fins", maintained by subsidence, in regulating tropical temperature and preventing a "runaway greenhouse effect." Spencer and Braswell [1997] compared new microwave humidity sounder data to General Circulation Model (GCM) analyses, discovering that the GCM humidity values in the free troposphere were overestimated in these dry regions. Zhang et al. [2003] noted the overall bimodality of tropical free tropospheric humidity, and that GCMs did not accurately represent the drier mode.

Despite their importance, however, no global climatology of the occurrence or sources of midlevel dry air layers exists. Other studies (Waugh and Polvani [2000], Waugh and Funatsu [2003], Ryoo et al. [2008]) provide climatologies on tropical upper-troposphere dry air intrusions originating in the stratosphere, but their analyses do not extend to the 0°C melting level where congestus tops commonly occur [Johnson et al. 1999]. Case studies have noted anomalously dry midtropospheric layers in the Indian Ocean [Zachariasse et al. 2001], but having a clearer picture of this global distribution

---

*Part of the data reported in this chapter is reprinted with permission from "Five-Year Climatology of Midtroposphere Dry Air Layers in Warm Tropical Ocean Regions as Viewed by AIRS/*Aqua*" by S.P.F. Casey, A.E. Dessler, and C. Schumacher, 2009. *J. Appl. Met. Clim.*, **48**, 1831-1842, Copyright 2009 by American Meteorological Society.

would not only enhance understanding of the limiting factors of congestus clouds, but also have greater implications for global warming theory. The next few chapters analyze the location, frequency, and source regions of dry air layers over the tropical oceans with an eye toward answering the following questions. What is the applicability of the previous Pacific Ocean regional case studies to the rest of the basin? Can these be applied to the Indian and Atlantic Oceans as well, or are there clear differences between the three basins? How does the distribution of such layers vary by season? Finally, where do these dry air layers originate, and how does this distribution vary seasonally?

To identify dry air layers, I again utilize the AIRS instrument onboard the *Aqua* satellite. Five years of near-continuous AIRX2RET version 5, level 2 data between September 2002 and August 2007 were used. As before, the study area is limited to those areas where the long-term monthly mean OLR is less than 240 W/m^2. This threshold reduces the study area to only those areas where deep convection is most prevalent (thus lowering the long-term mean OLR), and where the upper atmosphere would be expected to be the most humid given the prevalence of deep convective processes.

Figure 21 shows the frequency of occurrence at each pressure level for each level-2 relative humidity measurement with respect to liquid for $T > 273$ K and ice otherwise. In this and all following figures, observations at a given location and month were used only if the monthly mean OLR in that location and month was less than 240 W/m^2. The total values at each pressure level add up to 1. This figure shows that, though the air above the tropical oceans is normally very moist, there are occurrences of

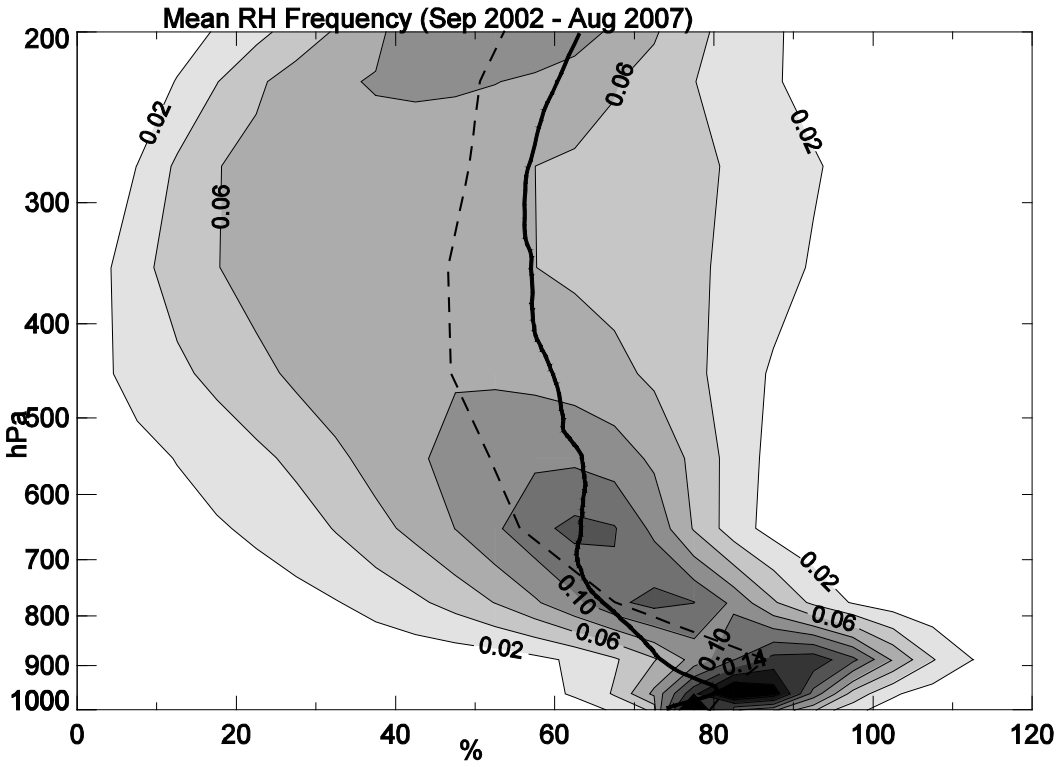

Figure 21. Relative frequency of mean relative humidity values over warm (mean monthly OLR < 240 W/m^2) oceanic regions, as a function of height. RH values are grouped into 5% bins, and vertical bin is based on pressure levels given in AIRS V5 data. The sum of all values at each pressure level adds to one. The vertical dashed line marks the mean profile. The thick solid line marks the mean profile from TOGA COARE, corrected for near-surface dry biases [Ciesielski et al. 2003]. Adapted from Casey et al. [2009], © American Meteorological Society. Reprinted with permission.

anomalously dry air. Plotted over this are the mean RH humidity profiles from the AIRS measurements (dashed) and from TOGA COARE (solid, Ciesielski et al. [2003]). These profiles suggest that, when taken over the full warm tropical maritime region, mean relative humidity values are lower between 600 and 400 hPa than during TOGA COARE, which was limited to the warm pool of the western Pacific.

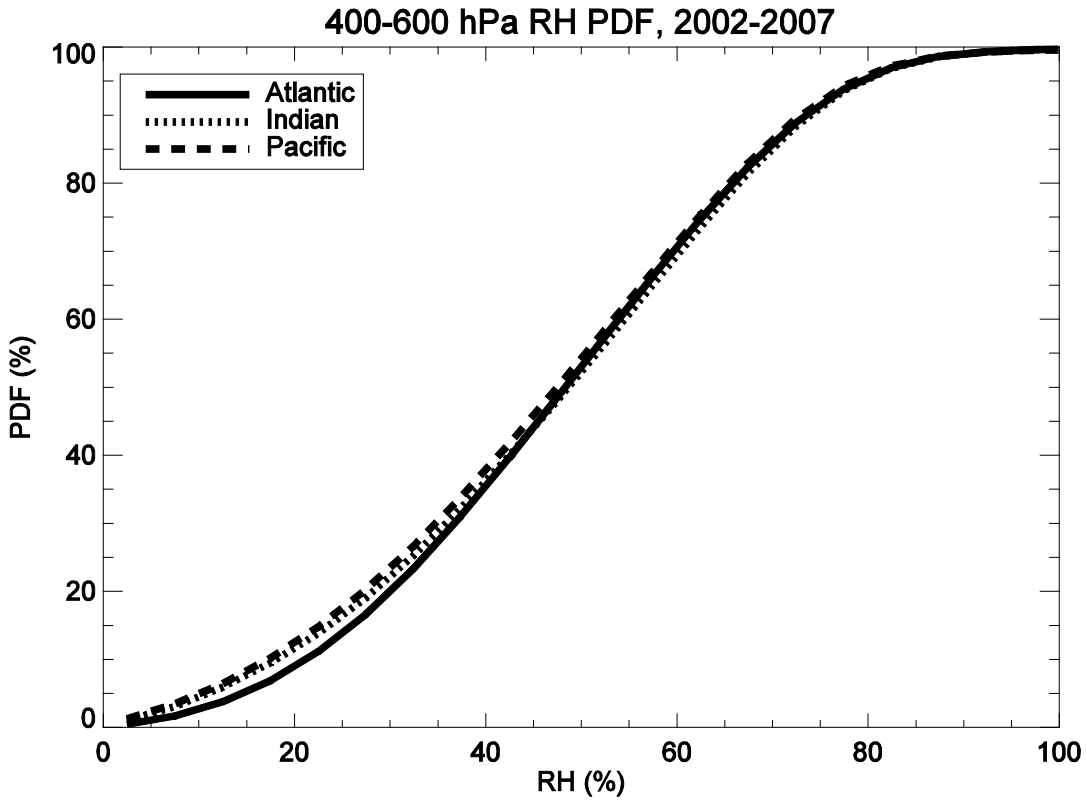

Figure 22. Cumulative Distribution Function of RH values between 400-600 hPa, separated into ocean basin.

Using relative humidity data over the eastern Pacific during the EPIC campaign, Zuidema et al. [2006] defined midlevel dry air layers as those instances where the relative humidity between 400 and 600 hPa was less than 40%. While 40% is a low value for midlevel relative humidity in Fig. 21, it is by no means anomalous. Brown and Zhang [1997] noted a range of 60% in midtroposphere RH during TOGA COARE between rainy and drought periods, with frequent observations at or below 20% RH during a drought period when lower cloud-top heights were more frequent. To analyze the driest relative humidity sources, while still using enough data to be statistically significant, we chose to analyze the lowest 10% of the data. Cumulative Density

Function (CDF) analysis (Figure 22) suggests that this 10% threshold is near relative humidity values of 20% in the Indian and Pacific Oceans and 25% in the Atlantic Ocean. To use the same threshold globally and given the greater area of the Indian and Pacific Oceans compared to the Atlantic, we decided to define dry air layers for this study as those areas where relative humidity at these altitudes was less than 20%, using the same pressure bounds (400 and 600 hPa) used by Zuidema et al. (2006). While this threshold is somewhat arbitrary, changes to the threshold (between 15-25%) suggested little change in the relative dry air layer distribution between ocean bodies. This threshold also coincides with the most frequent RH observations during dry periods noted by Brown and Zhang [1997].

CHAPTER IX

DRY AIR DISTRIBUTIONS*

Figure 23 shows the frequency of midlevel dry air layers over the tropical oceans, graphed into 2.5° grid resolution. The frequency is the number of dry air observations in a bin divided by the total number of AIRS observations within that bin times 100. The thick solid line marks the boundary of areas where the long-term mean OLR is less than 240 W/m^2 for at least one calendar month. Subsequent figures will focus on individual ocean basins. A similar color bar and contour system is used on each figure so as to make inter-figure comparisons easier.

A) Atlantic Ocean

Figure 23 shows that over the Atlantic Ocean, dry midlevel air is most frequently (i.e., ~25% of the time) observed around 12°N between 45°W and 25°W. Adjustment of the upper RH threshold between 15% and 25% revealed a range in the maximum frequency observation from 3.8% to 11.2%, as shown in Table 2. Otherwise, the frequency of dry air observations is low, around 5% over much of the Atlantic.

Figures 24-25 separates the total dry air distribution over the Atlantic by season. The maximum over the North Atlantic in September-November (SON; Figure 24a)

---

*Part of the data reported in this chapter is reprinted with permission from "Five-Year Climatology of Midtroposphere Dry Air Layers in Warm Tropical Ocean Regions as Viewed by AIRS/*Aqua*" by S.P.F. Casey, A.E. Dessler, and C. Schumacher, 2009. *J. Appl. Met. Clim.*, **48**, 1831-1842, Copyright 2009 by American Meteorological Society.

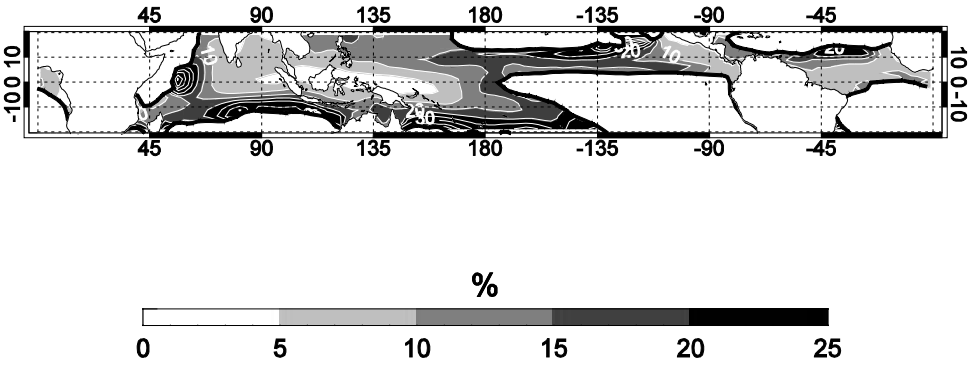

Figure 23. Frequency of midlevel dry air layers over the tropical oceans within each 2.5° bin. Shading marks each frequency change between 0 and 25%, with white contours marking further changes of every 5% (if applicable). The thick black line marks the maximum extent of where the monthly mean OLR for at least one month in the calendar year is less than 240 W/m^2; only those grid areas for which this criteria is satisfied have frequency contours provided. Adapted from Casey et al. [2009], © American Meteorological Society. Reprinted with permission.

corresponds well to that previously noted in Fig. 23. The region near 12°N and between 45° and 25°W only satisfies our low-OLR criteria in the months of October and November. NCEP wind reanalysis [Kalnay et al. 1996], overlain in Figure 24, shows that the long-term mean wind direction over this area at 500 hPa during SON is from the east-southeast, suggesting that wind flow at this height is climatologically from the African continent; the origins of these particular air parcels will be examined in further

Table 2. Probability that the midlevel (400-600 hPa) relative humidity (RH) measured over a given ocean basin will be less than the listed RH value (in percent).

P (RH <)	**Atlantic**	**Indian**	**Pacific**
15%	3.8	5.9	6.5
20%	6.9	9.5	10.3
25%	11.2	13.8	14.8

detail in section X. High occurrence of dry air is also seen in December-February (DJF; Figure 24b) closer to 8°N.

The frequency of dry air layers is much lower in March-May (MAM; Figure 25a) and June-August (JJA; Figure 25b). Mean 500 hPa winds during these months are from the east, similar to SON. In DJF, however, mean flow is more variable, with a winds south of 8°N from the east and those north of 8°N from the west.

The greater magnitude of dry air anomalies in SON also coincides with the farthest northward extent of our study area (i.e., long-term mean monthly OLR < 240 W/m^2). This would lead to a closer proximity of the study area to extratropical storm tracks in the subtropics (and even midlatitudes). It could then be postulated that the SON dry air anomalies are more likely to be related to extratropical influences than the other seasons, even though this is not suggested by the mean direction of flow for these months. This theory will also be tested in Section X.

B) Indian Ocean

Figure 23 shows a maximum in dry air frequency of ~50% over the western Indian Ocean (i.e., near the equator and around 57°E). High values from 20-40% are also noted in the southeast (around 12°S and 70°E-120°E). A large portion of the Indian

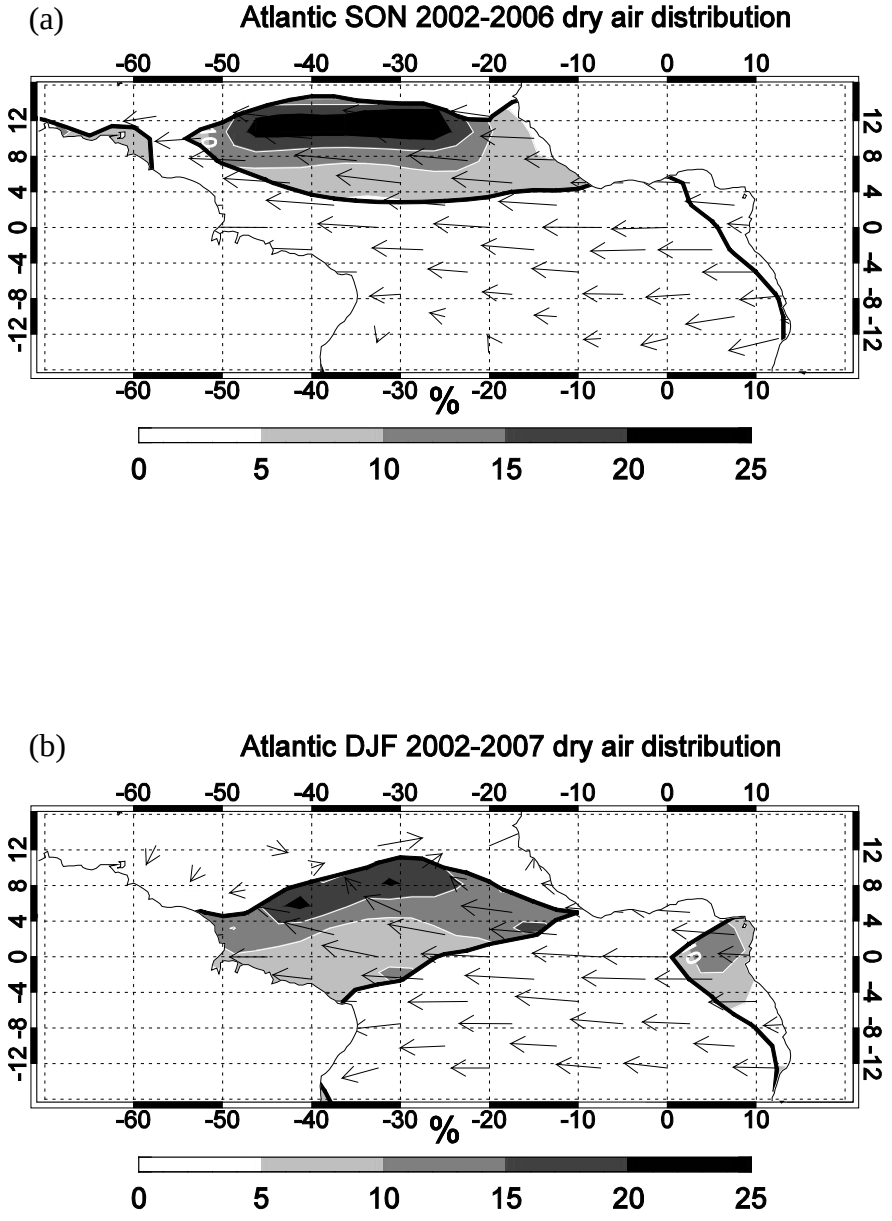

Figure 24. Frequency of midlevel dry air layers over the Atlantic Ocean in (a) September-November and (b) December-February within each 2.5° bin, with mean seasonal 500 hPa wind vectors overlain. Adapted from Casey et al. [2009], © American Meteorological Society. Reprinted with permission.

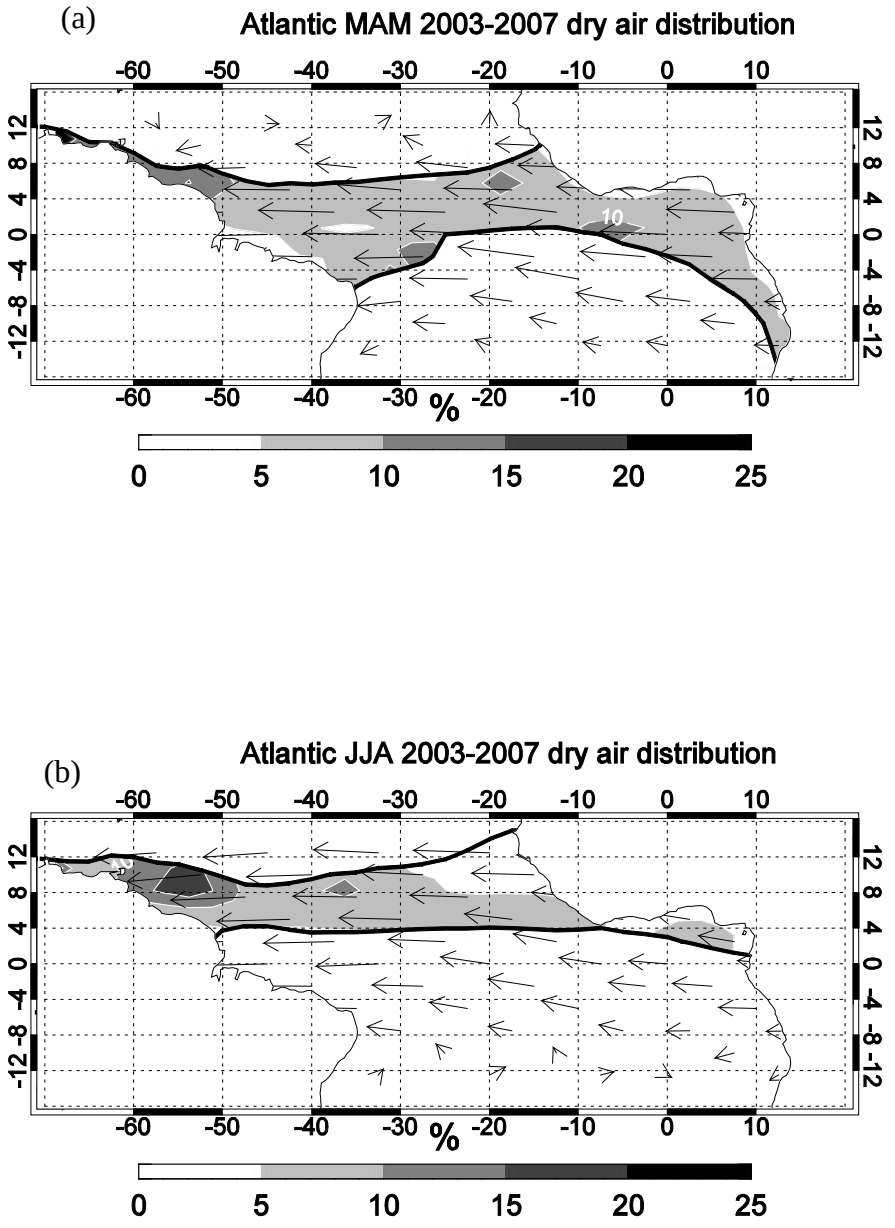

Figure 25. Frequency of midlevel dry air layers over the Atlantic Ocean in (a) March-May and (b) June-August within each 2.5° bin, with mean seasonal 500 hPa wind vectors overlain. Adapted from Casey et al. [2009], © American Meteorological Society. Reprinted with permission.

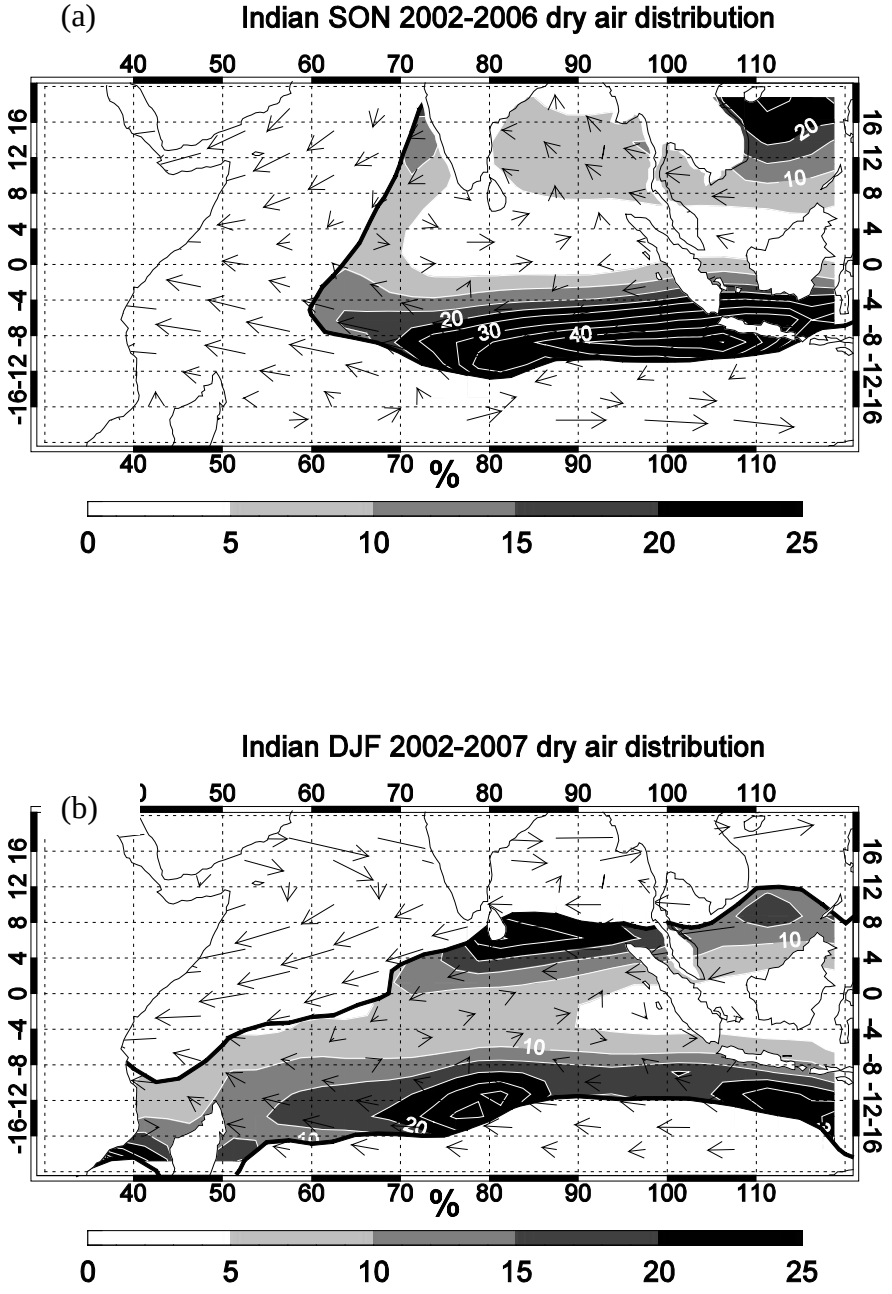

Figure 26. Frequency of midlevel dry air layers over the Indian Ocean in (a) September-November and (b) December-February within each 2.5° bin, with mean seasonal 500 hPa wind vectors overlain. Adapted from Casey et al. [2009], © American Meteorological Society. Reprinted with permission.

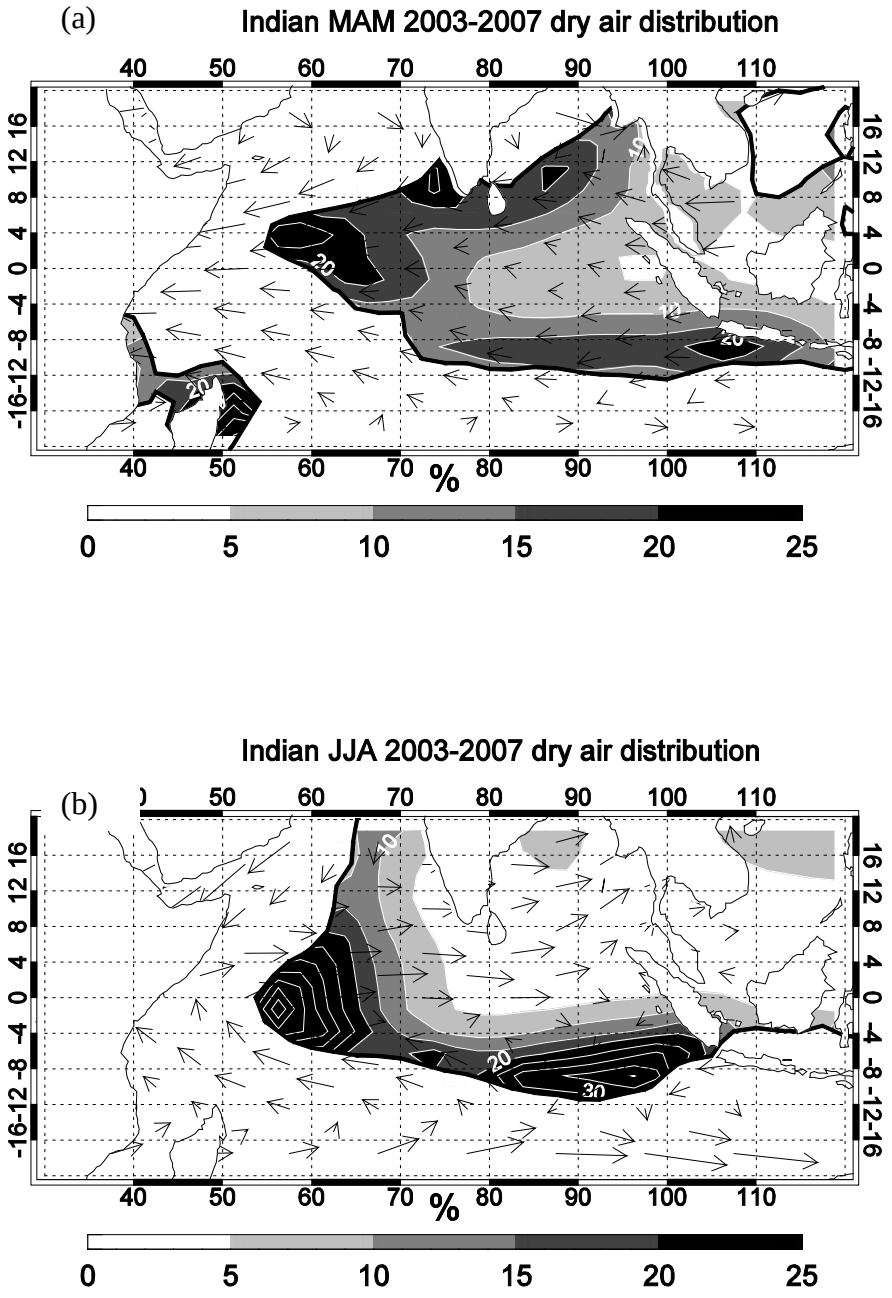

Figure 27. Frequency of midlevel dry air layers over the Indian Ocean in (a) March-May and (b) June-August within each 2.5° bin, with mean seasonal 500 hPa wind vectors overlain. Adapted from Casey et al. [2009], © American Meteorological Society. Reprinted with permission.

Ocean (from 4°S-20°N and 70°W-100°W) shows low occurrence of dry air observations.

Figures 26-27 show the largest dry air maxima in JJA (Figure 27b) and SON (Figure 26a), with smaller frequencies noted in DJF (Figure 26b) and MAM (Figure 27a). The months June-November also happen to be when the Madden-Julian Oscillation (MJO) signal is weaker [Madden and Julian 1994]. This may be related to the warming and drying of the mid-troposphere following the active phase of the MJO, as reported by Tian et al. [2006]. In comparison with Figure 23, it is clear that the western Indian Ocean peak is mostly due to layers in JJA (the active monsoon season), while the southeastern peak is strongest in SON. Though substantially lower in magnitude than those in June-November, minor peaks are noted in DJF near Sri Lanka and around 12°S, 80°E, as well as in MAM over 4°N, 60°E and off the coast of Madagascar. It should be noted that these lower values are comparable to what constitutes a high concentration of dry air layers in the Atlantic (Figures 24-25) due to the lower occurrence of dry air layers overall over the Atlantic vs. the Indian Ocean.

C) Pacific Ocean

Figure 23 shows high dry air frequencies of ~30% over the central Pacific in the Intertropical Convergence Zone (ITCZ) and close to 20°S in the South Pacific Convergence Zone (SPCZ). Fewer dry air layers are observed close to the equator, where easterlies remain prevalent at 500 hPa year-round (Figures 28-29). Closer to the subtropics, westerlies are seen more frequently depending on the extent of the

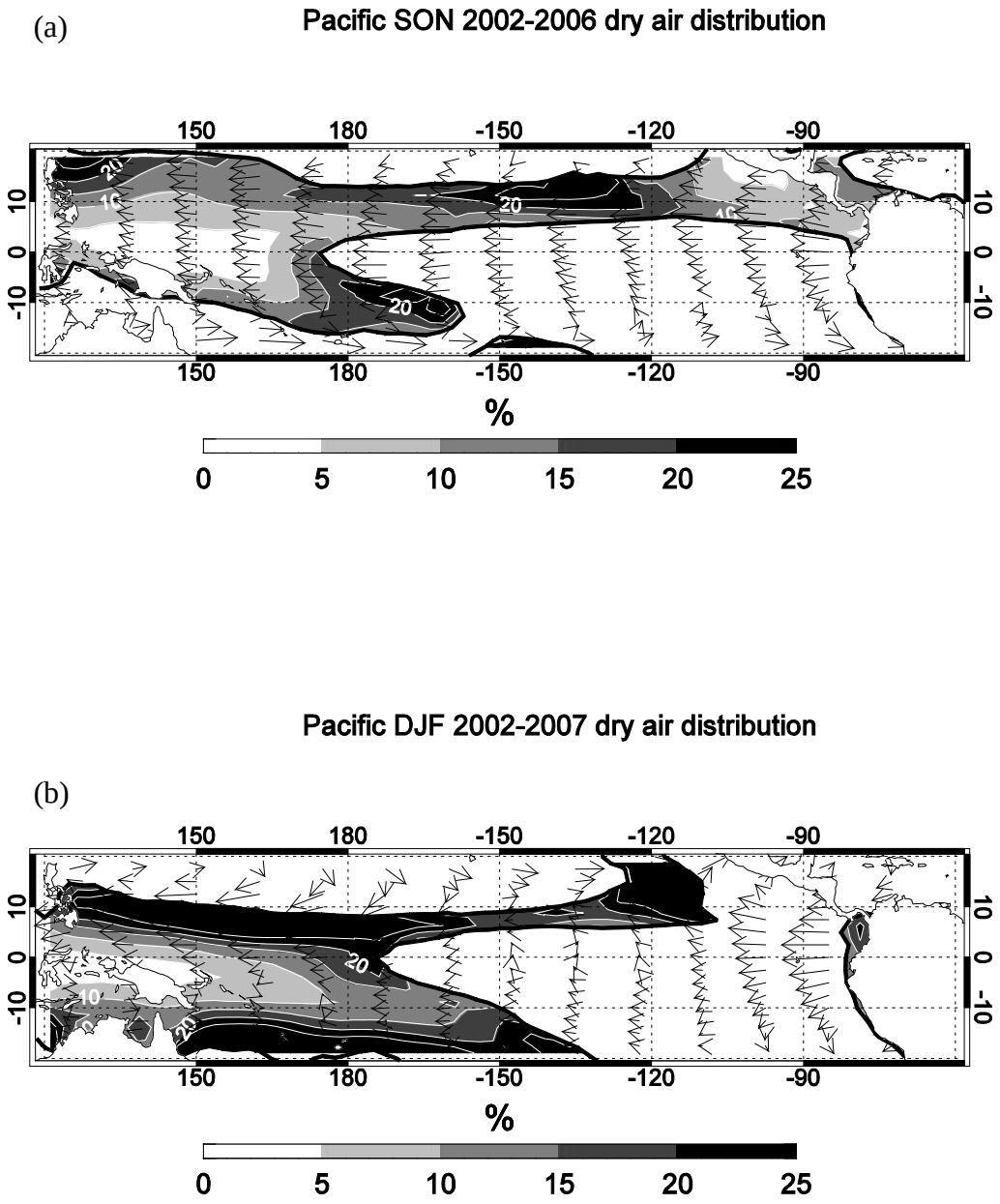

Figure 28. Frequency of midlevel dry air layers over the Pacific Ocean in (a) September-November and (b) December-February within each 2.5° bin, with mean seasonal 500 hPa wind vectors overlain. Adapted from Casey et al. [2009], © American Meteorological Society. Reprinted with permission.

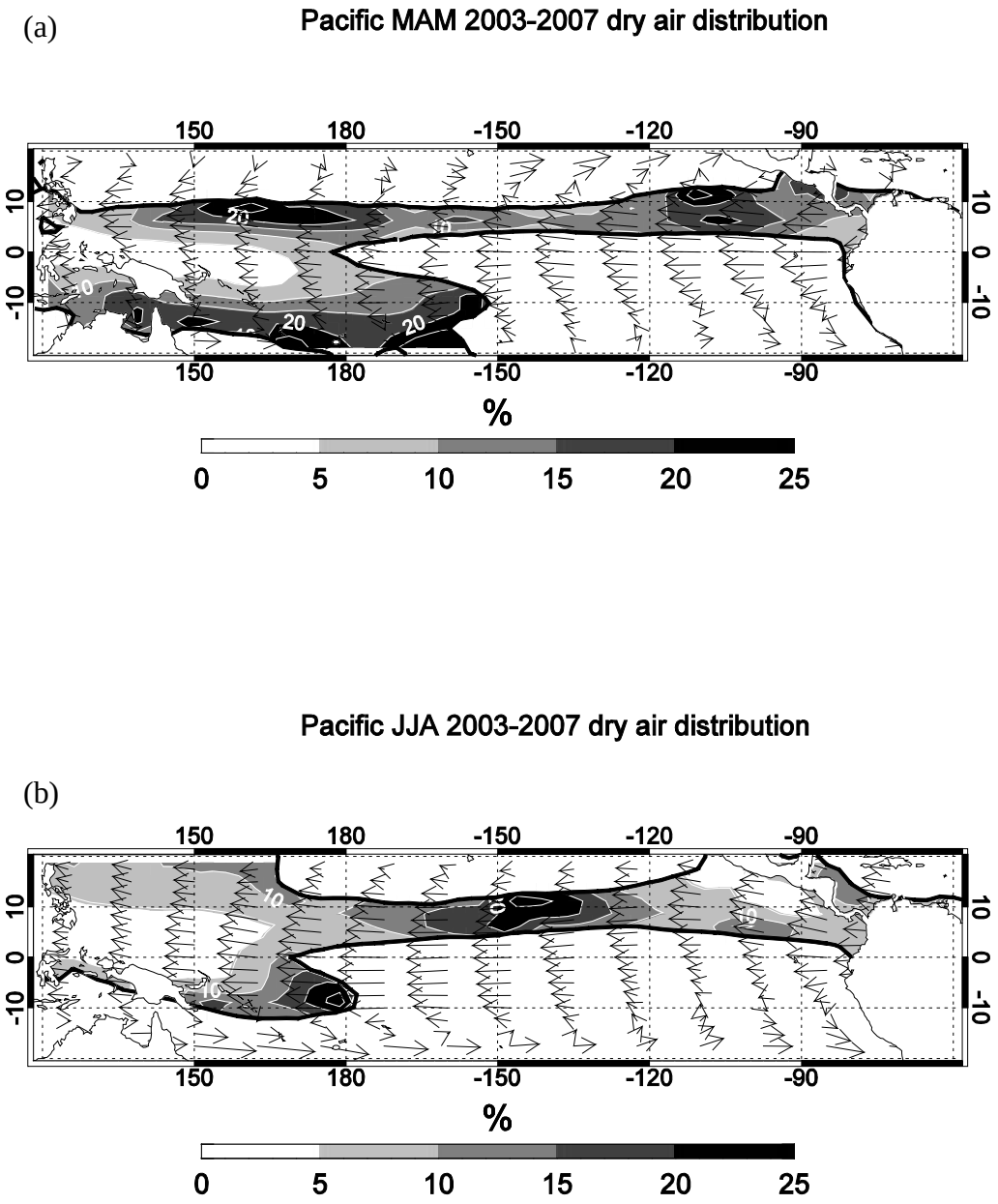

Figure 29. Frequency of midlevel dry air layers over the Pacific Ocean in (a) March-May and (b) June-August within each 2.5° bin, with mean seasonal 500 hPa wind vectors overlain. Adapted from Casey et al. [2009], © American Meteorological Society. Reprinted with permission.

tropical/subtropical boundary. The relation between westerlies and dry air layers will be discussed in the next section. Overall, dry air layers appear to be present at least 10% of the time basin-wide, except in the far east Pacific and over the warm pool region of the western Pacific.

Figures 28-29 show that the highest frequency of dry air layers is in DJF (Figure 28b), with smaller frequencies in the other seasons. Areas of maximum occurrence in SON (Figure 28a) are in the central Pacific, north of the Philippines, and along the eastern edge of the SPCZ. During the EPIC campaign [Zuidema et al. 2006], the R/V Ronald Brown was located at 10°N, 95°W during the month of September; Figure 28a shows that dry air layers occur in this region 5% of the time during SON. In DJF, maximum values are seen in a long swath near 10°N, 120°E-160°W, along the southern boundary near 20°S, 150°E-140°W, and in the east Pacific near 10°N, 120°W. The TOGA COARE field program observing period was from 1 November 1992 to 28 February 1993, over a region roughly bounded by 140°E, 180°, 10°S and 10°N [Webster and Lukas 1992]; Figure 28b shows that the frequency of dry air layers varies greatly in this region, from 0-35% occurrence. Observations in MAM (Figure 29a) remained roughly in the same areas as DJF, though the magnitudes were substantially decreased.

In JJA (Figure 29b), only two weak maxima are noted, one near 10°S, 180°E and another near 10°N, 150°W. The mean 500-hPa flow across the 10°N latitude during JJA is largely from the east. However, over the 150°W longitude, the winds have a slight southward component (i.e., from the subtropics), while the winds from areas to the east and west have a slight northward component. Meanwhile, winds south of the SPCZ

maximum shift from eastward (near 20°S) to westward (near 10°S). This shift within a close proximity on a climatological scale suggests a greater opportunity for mixing of tropical and extratropical air in this location, suggesting that dry air layers over the area during austral winter may originate in the extratropics.

CHAPTER X

LOCATIONS OF DEHYDRATION*

Trajectories backwards in time from observation to twenty days prior were calculated for each midlevel dry air region using a trajectory program using 3D NCEP winds as described in Bowman [1993]. Trajectories were initialized at the location of each dry retrieval in AIRS version 5, at 500 hPa in height and 0000 UTC. We calculate relative humidity for each time step of the trajectory using the AIRS-measured value at the end of the trajectory and NCEP temperature interpolated to each time step (six hours back in time). While AIRS also provides temperature measurements, the nature of back-trajectory analysis requires temperatures at specific points and times along the trajectory, something that AIRS is not able to provide given its orbit; therefore, the NCEP temperature is used. Our goal is to find the most recent time when each trajectory was saturated (i.e., reached 100% RH). If we assume that this is the last time condensation occurred, then this point is the location where the parcel's humidity was set. This is a well-validated approach to estimating tropical water vapor (see Dessler and Minschwaner [2007] and references therein). While individual AIRS measurements, as mentioned before, are accurate within ~10%, Dessler and Sherwood [2000], while using a similar model, noted that errors may also arise from physical processes not included in

---

*Part of the data reported in this chapter is reprinted with permission from "Five-Year Climatology of Midtroposphere Dry Air Layers in Warm Tropical Ocean Regions as Viewed by AIRS/*Aqua*" by S.P.F. Casey, A.E. Dessler, and C. Schumacher, 2009. *J. Appl. Met. Clim.*, **48**, 1831-1842, Copyright 2009 by American Meteorological Society.

the model, errors in the NCEP wind and temperature fields, and/or unresolved motions in the wind fields. Dessler and Sherwood [2000], however, also noted that situations arising from these did not lead to serious systematic errors.

Figure 30 shows two sample backtrajectories calculated from this method, using observations over the Atlantic Ocean in September 2002. Stars at the end of the trajectory mark the location of observation by AIRS. Thick black lines mark where the long-term mean OLR for September is less than 240 W/m^2, and thin black lines mark the country outlines for geographical reference. This figure shows that, though the locations for observation are similar for the two, the source regions are very different. On the top, the backtrajectory path goes to the northeast, ending over Libya. On the bottom, the path goes to the southeast, with a location of dehydration identified over the southern Atlantic.

Figure 31 shows the relative frequency of time from saturation to observation, separated by season. The area under each curve integrates to one. It appears that the mean time since saturation is five days, with an exponential drop-off into longer time-periods. The trajectories were only processed out to 20 days for computational reasons, though it appears that for about 10% of the backtrajectories, the air parcels had not yet reached saturation by this time. It is clear that the time from saturation to observation is about five to six days from September through to May, while the maximum time period from June-August is seven days, with many more trajectories lasting for ten days or more.

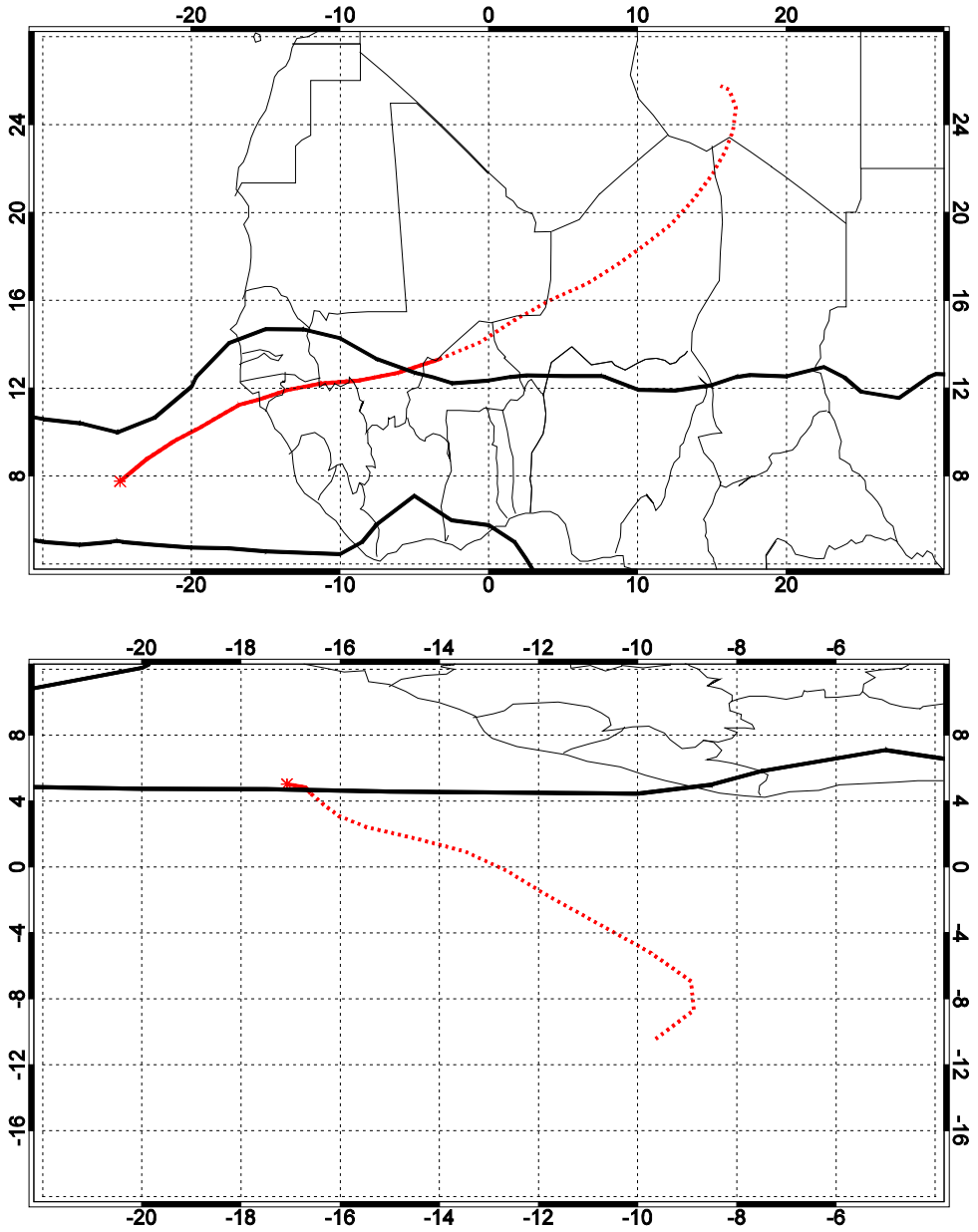

Figure 30. Two sample calculated backtrajectories calculated from observations over the Atlantic Ocean in September 2002. Stars at the end of the trajectory mark the location of observation by AIRS. Thick black lines mark where the long-term mean OLR for September is less than 240 W/m^2, and thin black lines mark country outlines for geographical reference. Dashed red line marks the trajectory path where the long-term mean OLR for June is greater than 240 W/m^2. Adapted from Casey et al. [2009], © American Meteorological Society. Reprinted with permission.

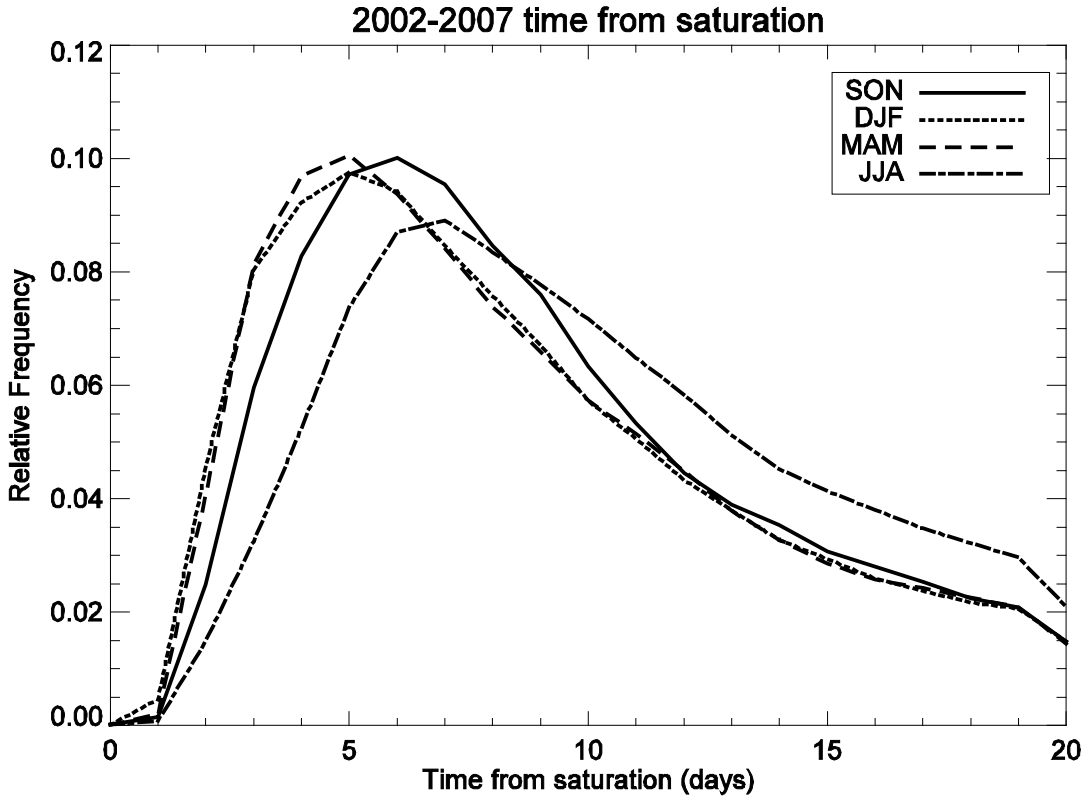

Figure 31. Relative frequency distribution of the time between parcel saturation to observation, binned by day and separated by season. The sum under each curve equals unity. Adapted from Casey et al. [2009], © American Meteorological Society. Reprinted with permission.

The greatest number of JJA dry air observations comes from the Indian Ocean, where according to Figure 27b, most are viewed southwest of Sumatra and southeast of Somalia. The 500 hPa JJA winds near Sumatra are typically light, which would allow dry air layers to remain dry in the absence of turbulent mixing, allowing them to be viewed multiple times by the *Aqua* satellite as they slowly drift westward. Winds typically increase near 80°W, shifting from a westward trajectory to northwestward and then to a northward trajectory. This path may bring these dry air layers directly into the second identified location of dry air noted off the Somali coast, thus sampling the same

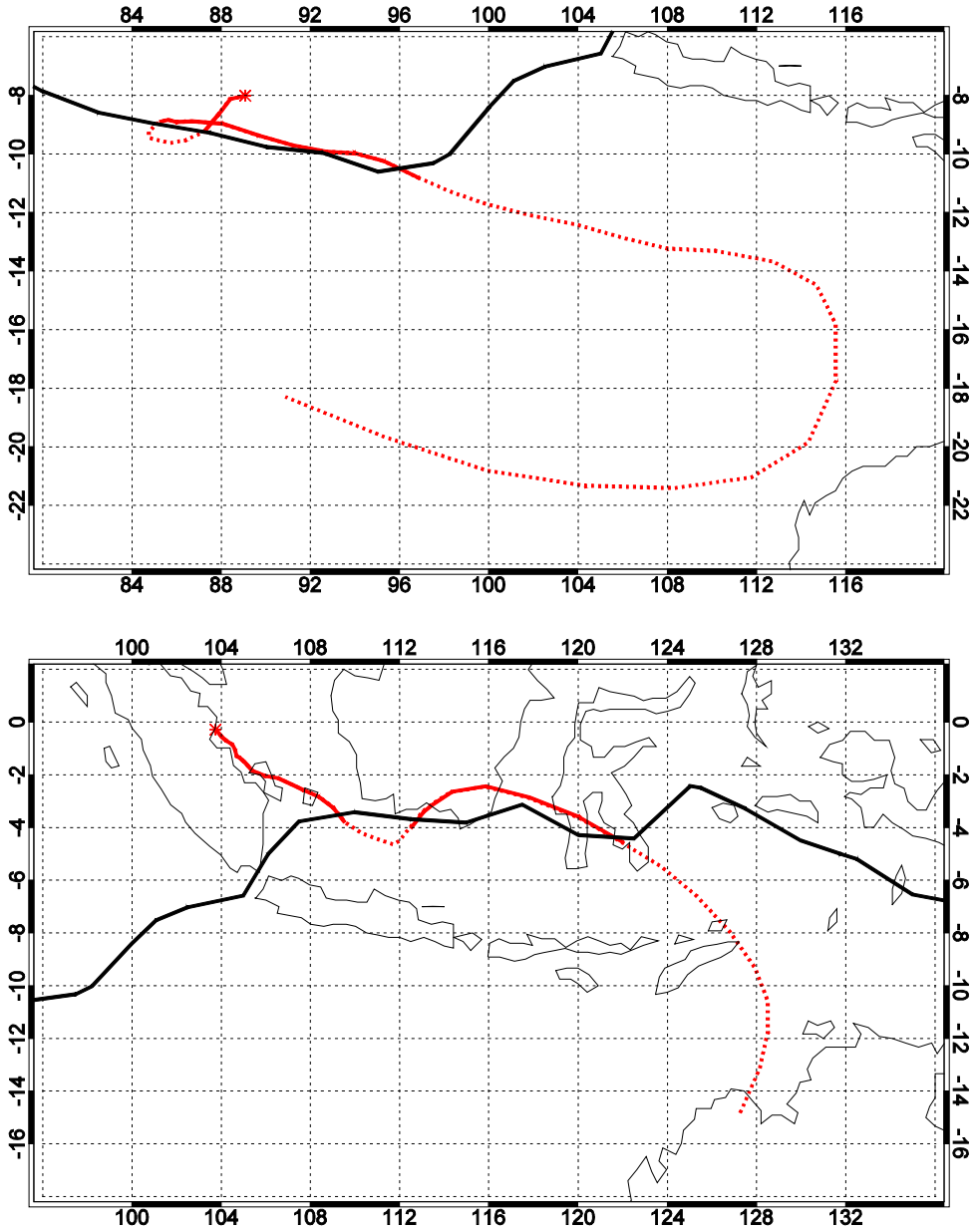

Figure 32. Two sample calculated backtrajectories calculated from observations over the Indian Ocean in June 2003. Adapted from Casey et al. [2009], © American Meteorological Society. Reprinted with permission.

feature in additional overpasses. Upon investigation of this (not shown), it was noted that 1/3 of Indian Ocean JJA backtrajectories were sampled twice. Two such trajectories from June 2003 are shown for reference in Figure 32. This combination of light wind

conditions and the potential for multiple sampling is only seen in the Indian Ocean during JJA, and is not seen in the other two ocean basins. This suggests that the longer time between saturation and observation during JJA than the other seasons can be traced back to Indian Ocean conditions during these three months.

To answer the question of whether these dry layers were last saturated over land or ocean, a simple land/ocean mask was checked at the location of dehydration identified via trajectory analysis. Table 3 lists the percentage of dry air observations that were last saturated over the ocean. This table shows that, in every ocean basin and every season, oceanic origins are more common than land origins. The Indian and Pacific Oceans have dry air layers originating from ocean regions 70.1% and 81.4% of the time, respectively. A higher percentage of oceanic sources for the Pacific Ocean would be expected, given the larger size of this basin. The Atlantic Ocean, by contrast, has both the lowest percentage of oceanic origins (69.1%) and the greatest spread between seasons, with nearly 40% of dry air parcels being last saturated over land during JJA.

A) Atlantic Ocean

The shading in Figures 33-34 indicates the relative locations of dehydration for parcels originating over the Atlantic Ocean, separated into season and binned into 15°x15° boxes. The total of all values in shading add up to unity. Mean trajectories are computed from the center of each 15°x15° box that contributes at least 1% of the total observed midlevel dry air layers. These mean trajectories are plotted in red.

Table 3. Percentage of dry air observations that originate over oceanic regions. Adapted from Casey et al. [2009], © American Meteorological Society. Reprinted with permission.

	Atlantic	**Indian**	**Pacific**
SON	80.8%	69.1%	83.7%
DJF	69.8%	73.9%	77.4%
MAM	63.9%	66.6%	75.7%
JJA	61.8%	70.8%	88.6%

In boreal autumn and winter (Fig. 33), the shading indicates that most dry air layers originate in the Northern Atlantic. In boreal spring and summer (Fig. 34), the Southeastern Atlantic is a more prominent source region. The 500 hPa winds from March-August over this region have a more northward component than those from September-February, thus bringing air towards the equator rather than simply towards the west. In addition, layers originate from North Africa during all seasons. Galewsky et al. [2005] and Dessler and Minschwaner [2007] identified similar trajectories in the North Atlantic and North Africa to be parcels riding up the isentropes and cooling as they mix reversibly into mid-latitudes. This tropical air then condenses and loses water; when it then returns to the tropical regions, the air is drier than it was when it left.

The mean trajectories that originate in the North Atlantic travel mostly southward in SON, move more southeastward in DJF and MAM and travel little in JJA. Comparing Figures 24-25 and 33-34, it is apparent that, with the exception of DJF, these parcel backtrajectories from the North Atlantic do not coincide with time periods where the climatological mean 500-hPa winds are from the north. This suggests that many of

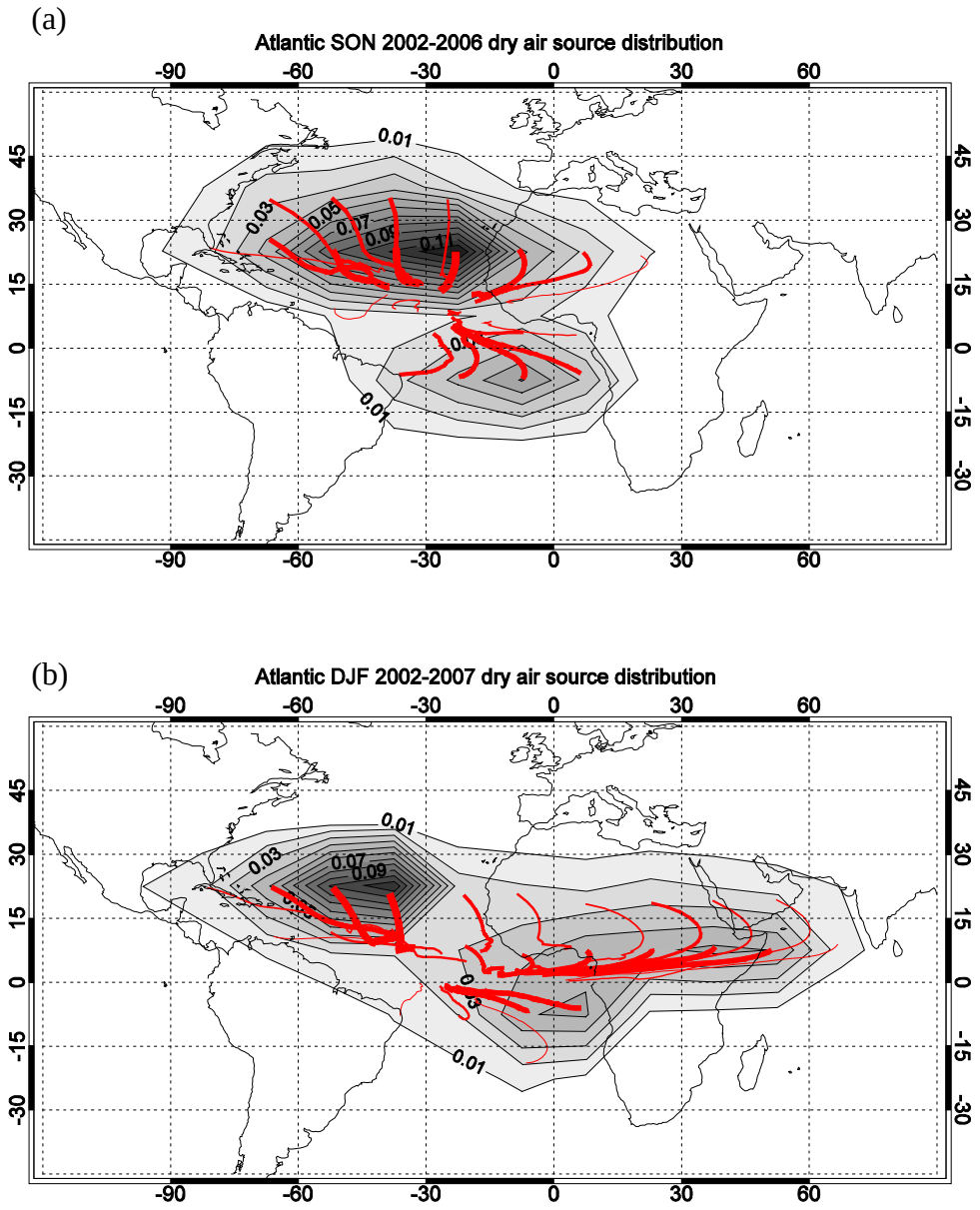

Figure 33. Relative frequency of dry air layer source regions for the Atlantic Ocean, grouped into 15° bins and separated into (a) September-November and (b) December-February. The sum of all contoured values add to unity. Red lines mark the mean trajectory from each bin where the relative frequency is greater than 1%. The thickness of each red line is proportional to the relative frequency from the associated bin. Adapted from Casey et al. [2009], © American Meteorological Society. Reprinted with permission.

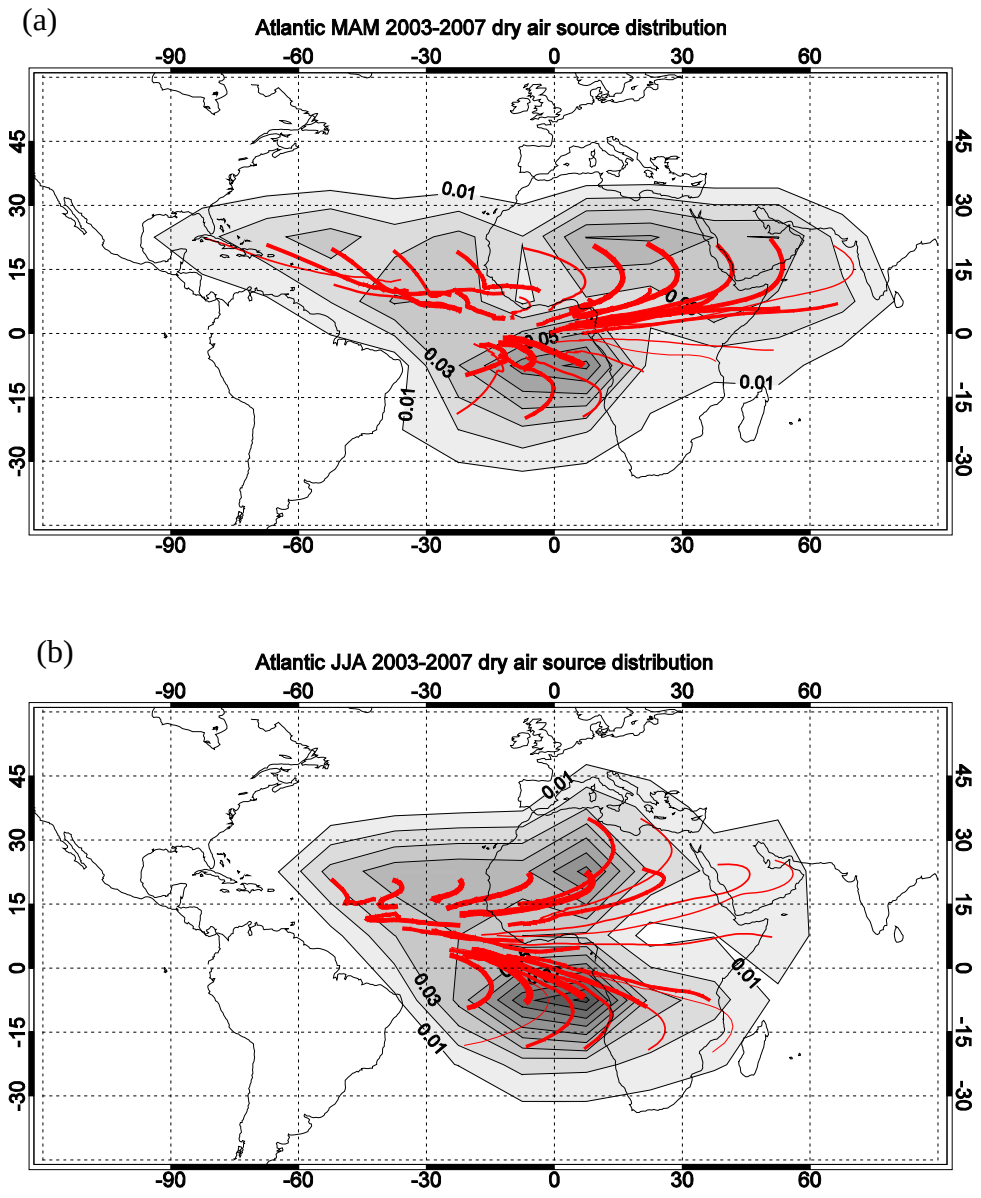

Figure 34. Relative frequency of dry air layer source regions for the Atlantic Ocean, grouped into 15° bins and separated into (a) March-May and (b) June-August. Adapted from Casey et al. [2009], © American Meteorological Society. Reprinted with permission.

the studied backtrajectories do not coincide with climatological mean winds, lending credence to the argument that these observations of very dry air are anomalous.

The mean trajectories that originate in the South Atlantic travel northwestward, with pronounced curves around 15°S where the climatological winds change from northwestward to northeastward. This shift from midlatitude westerlies to tropical easterlies is also evident in the trajectories originating in East Africa. In DJF and MAM, the East African mean trajectories appear to converge from their varied origins into a close grouping just north of the Equator.

B) Indian Ocean

Figures 35-36 show that, regardless of season, the majority of dry air layers entering the Indian Ocean come from the southern subtropical ocean. Trajectory analysis of the layers originating in the South Indian Ocean shows largely northeastward transport until about 15°S, when the winds shift to northwestward. The endpoints of the average trajectories for SON (Figure 35a) and JJA (Figure 36b) point towards the eastern and western Indian Ocean, respectively. Southeastward flow between Indonesia and Australia during JJA may "block" flow from the extratropics west of 90°E, whereas more northerly flow west of 90°E allows more extratropical air to travel into the tropics.

More variety is seen in the endpoints of the trajectories of the layers from the north. In SON layers generally move eastward into the South China Sea (included in this paper as part of the Indian Ocean due to geographic convenience). From December-May, Northern Hemisphere trajectories move southeastward into the Bay of Bengal [mostly in DJF (Figure 35b)] and peninsular India [mostly in MAM (Figure 36a)]. Northern Indian Ocean dry air layers originate predominantly over the Arabian Sea. Table 4 shows that more dry air layers are noted in May than in any other month,

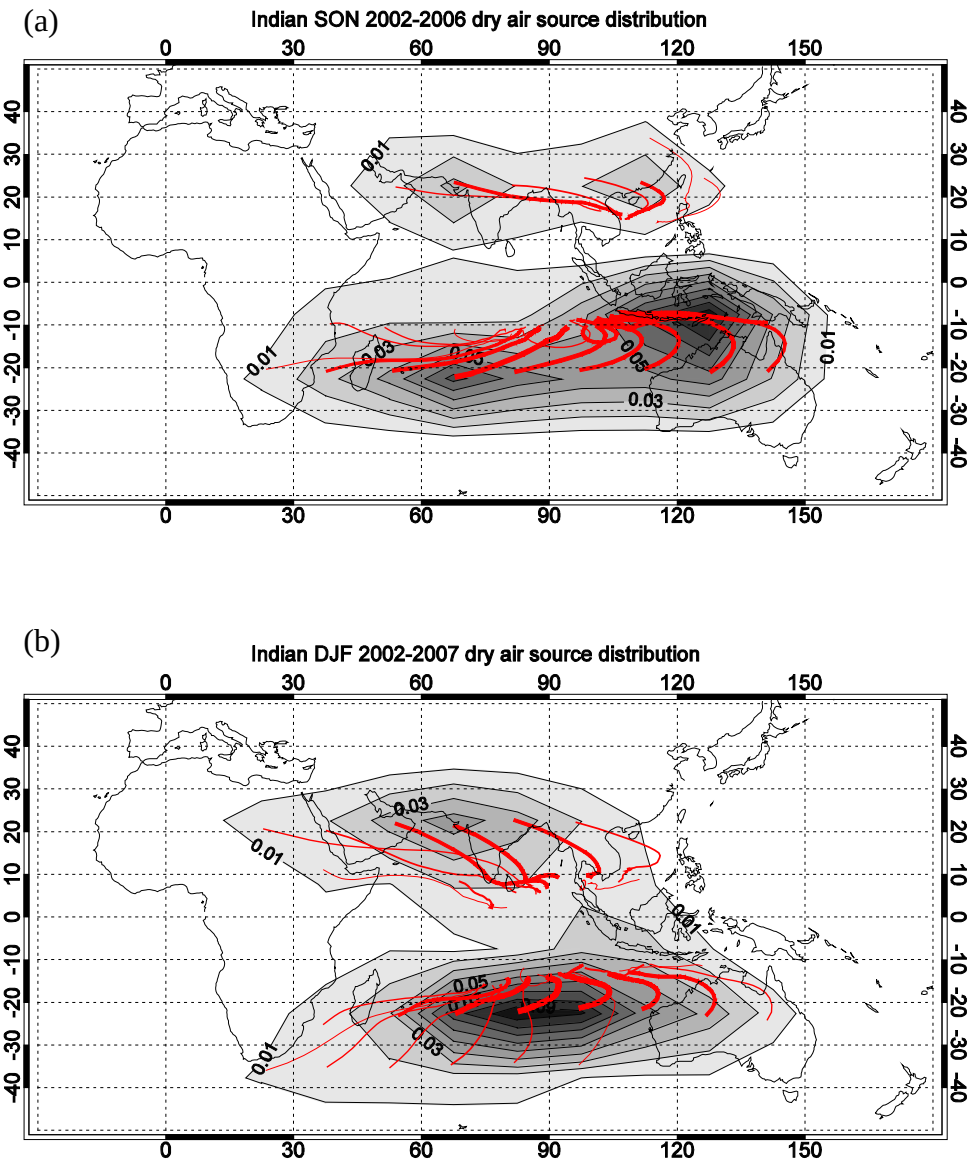

Figure 35. Relative frequency of dry air layer source regions for the Indian Ocean, grouped into 15° bins and separated into (a) September-November and (b) December-February. Adapted from Casey et al. [2009], © American Meteorological Society. Reprinted with permission.

including more intrusions than March and April combined; therefore, Figure 36a is mostly dominated by intrusions in the month of May. This high count is followed by

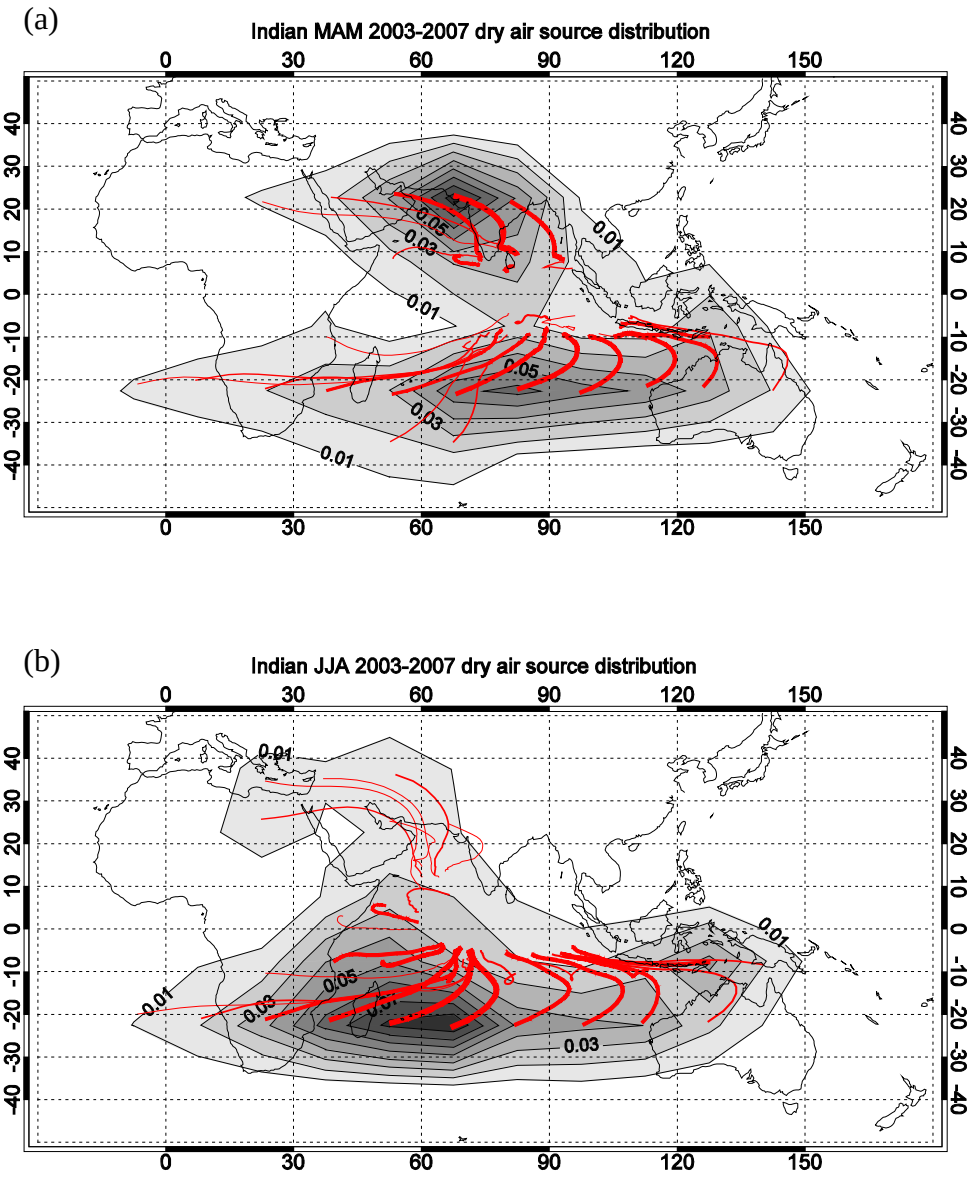

Figure 36. Relative frequency of dry air layer source regions for the Indian Ocean, grouped into 15° bins and separated into (a) March-May and (b) June-August. Adapted from Casey et al. [2009], © American Meteorological Society. Reprinted with permission.

much lower counts in boreal summer, most likely resulting from the oceanic flow northward onto the Indian subcontinent during the monsoon months. The onset of the

Table 4. Number of discernable dry air trajectories in the Indian Ocean, separated by month.

January	45968
February	47783
March	21020
April	26004
May	78002
June	44692
July	45355
August	55234
September	43527
October	74519
November	59435
December	45033

monsoon in June is very apparent, as seen in the low-count trajectories originating from the Middle East, curving southward before reaching peninsular India, and ending in the Arabian Sea.

C) Pacific Ocean

Figures 37-38 shading shows that there is a greater spread in the locations of dry air origin over the Pacific than in the previous two ocean basins. This, however, is mostly because the Pacific is a larger basin. The North and East Pacific predominate as source regions throughout the year. Dry air frequently originates in Australia, especially from December-May. Lower frequencies are seen from the southeast Pacific, South and Southeast Asia, and the Caribbean Sea.

The first interesting feature of the mean trajectories is the grouping of mean trajectories from South and Southeast Asia in each season except JJA (Figure 38b). Parcels along these trajectories travel along the subtropical jet around 20°N until around 150°E, where 500 hPa flow is climatologically southward these times of the year. Upon

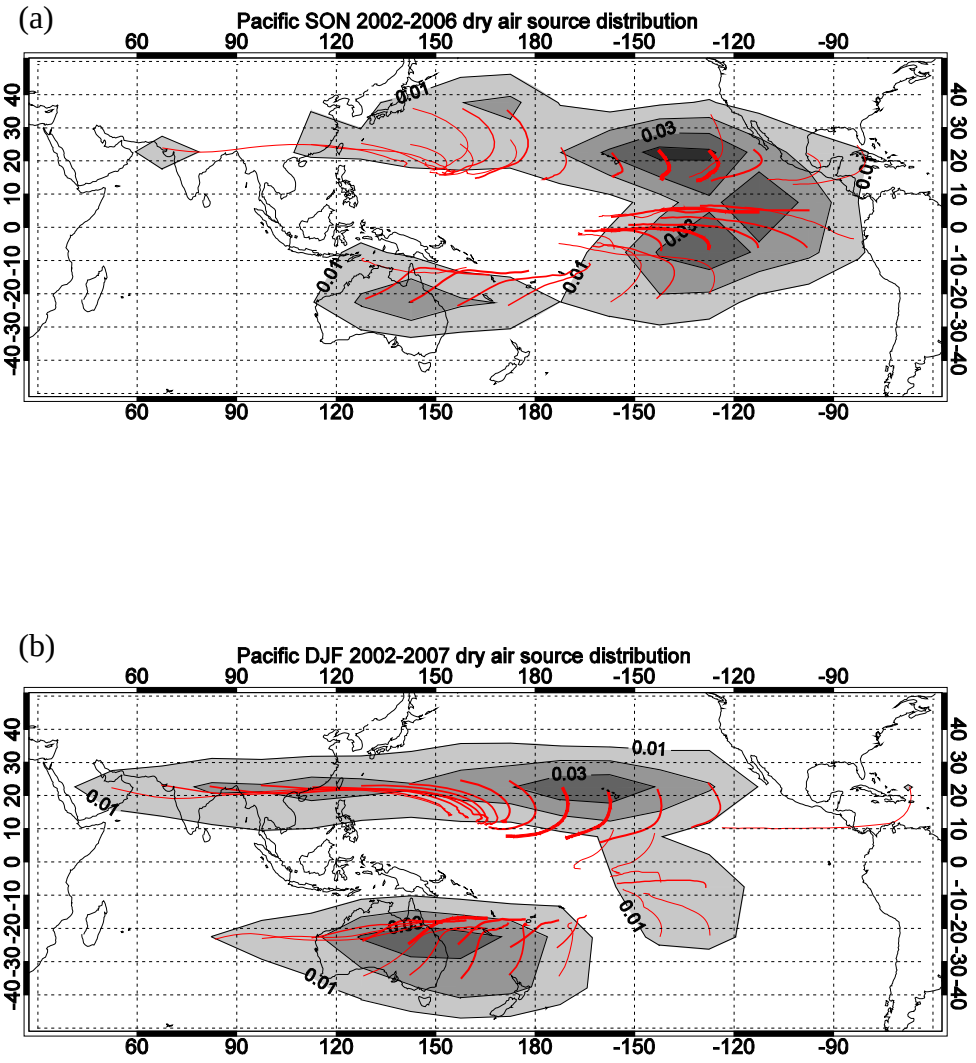

Figure 37. Relative frequency of dry air layer source regions for the Pacific Ocean, grouped into 15° bins and separated into (a) September-November and (b) December-February. Adapted from Casey et al. [2009], © American Meteorological Society. Reprinted with permission.

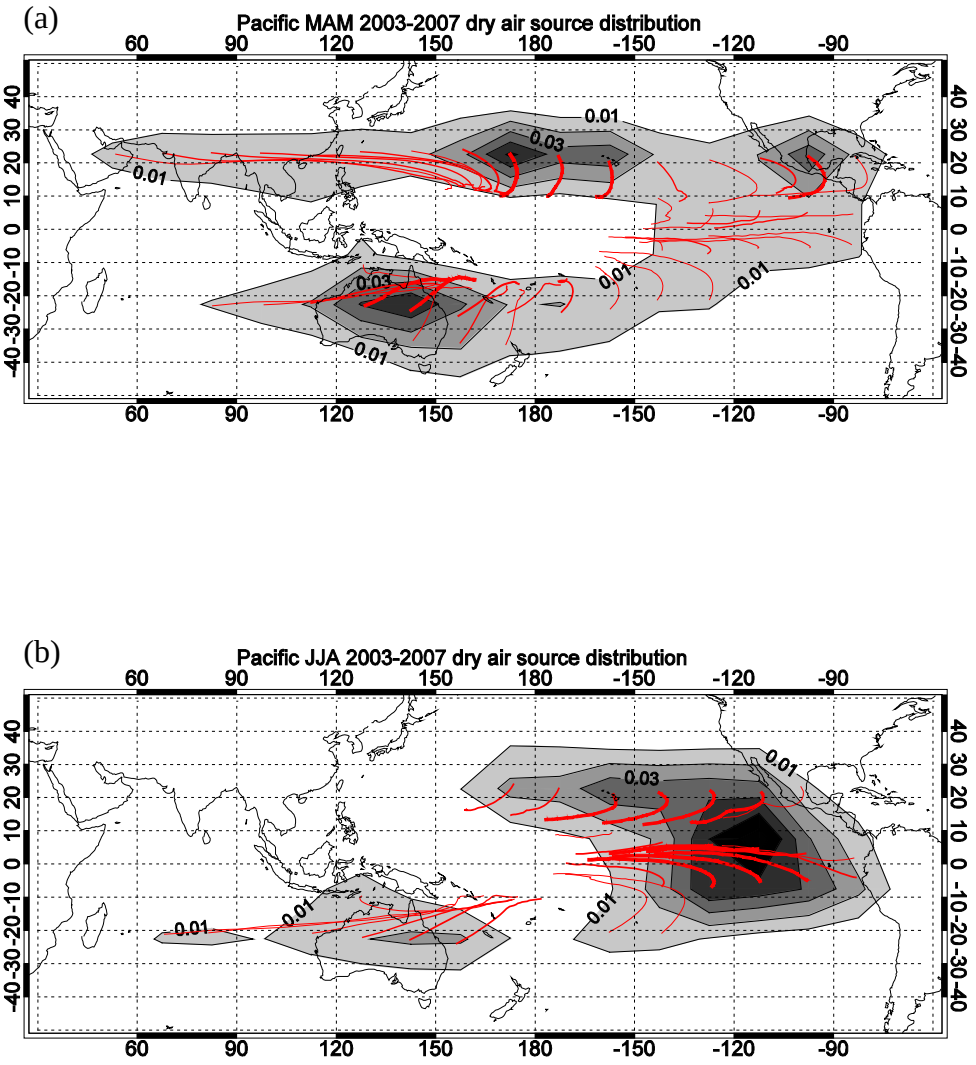

Figure 38. Relative frequency of dry air layer source regions for the Pacific Ocean, grouped into 15° bins and separated into (a) March-May and (b) June-August. Adapted from Casey et al. [2009], © American Meteorological Society. Reprinted with permission.

encountering this flow, the parcels curve southeastward and settle into the northwest Pacific. Redelsperger et al. [2002], as mentioned in the introduction, analyzed dry air

layers observed during TOGA COARE. Looking at Figure 37, focusing on this region (140°W to 180°, 10°S to 10°N) during DJF (Figure 37b), mean trajectories enter this region predominantly from the north. While more tropical convection was noted during TOGA COARE in the southern half of the study area, no mean trajectories enter this region from the southern half. Thus, Figure 37 suggests that the dry air layers analyzed during TOGA COARE may have originated in south and/or southeast Asia before entering the study area from the north.

Trajectories from the North Pacific appear to slowly move southward, with some of the trajectories showing clear southwestward curves. The curve is more prominent in trajectories from the Caribbean Sea, with the trajectories ending along a westward track as the parcels settle in the East Pacific. Zuidema et al. [2006] calculated two back trajectories (20 and 22 September 2001) initialized at 10°N, 95°W, where the R/V Ronald H. Brown was located during the EPIC campaign. The trajectory for 20 September tracked east-northeast towards Central America; this would seem to agree with a mean trajectory traveling from the Caribbean, as seen in SON according to Figure 37a. The 22 September trajectory tracked south towards the equator; not precisely in line with our calculated mean back-trajectories, but close enough so that this 22 September case should not be seen as anomalous.

Trajectories originating over Australia move north and northeastward into the SPCZ. Many endpoints of the mean trajectories from the Southeast Pacific appear to end in the Central Pacific, in an area not included in the dry air distribution analysis (compare to the bold OLR outline in Figure 23). Parcels originating from these

Southeast Pacific regions appear to disperse evenly between towards the ITCZ and toward the SPCZ, leaving a mean trajectory pointing to the area in between.

CHAPTER XI

DISCUSSION OF DRY AIR LAYERS*

Whereas previous studies have noted midlevel dry air layers over specific regions in the Pacific Ocean based on case studies, the previous sections looked at all warm oceanic areas using the criteria that, for at least one month, the monthly mean OLR over that area is less than 240 W/m^2. I used a definition of dry air layers of RH < 20%. Now I'll revisit the questions raised in Chapter VIII:

- *What is the applicability of the previous Pacific Ocean regional case studies to the rest of the basin?*

Large variations in the spatial and seasonal distribution of midlevel dry air layers exist across the Pacific. This high degree of variation suggests limits on the applicability of case-study trends and observations of dry air layers to the Pacific as a whole. While field campaigns such as TOGA COARE and EPIC have contributed greatly to our understanding of tropical meteorology, studies may be needed in other regions to describe more accurately the regional nature and effects of midlevel dry air layers.

- *Can these be applied to the Indian and Atlantic Oceans as well, or are there clear differences between the three basins?*

---

*Part of the data reported in this chapter is reprinted with permission from "Five-Year Climatology of Midtroposphere Dry Air Layers in Warm Tropical Ocean Regions as Viewed by AIRS/*Aqua*" by S.P.F. Casey, A.E. Dessler, and C. Schumacher, 2009. *J. Appl. Met. Clim.*, **48**, 1831-1842, Copyright 2009 by American Meteorological Society.

Compared to the Pacific Ocean, the Indian Ocean has a similar dry air CDF, and both basins see relatively fewer dry air layers in MAM when extratropical-to-tropical winds are seen climatologically only in localized areas such as the Indian Subcontinent, Australia, and near 10°N, 160°E. However, the spatial distribution of layers appears to be more localized in the Indian Ocean, with maxima approaching 50% occurrence in SON and JJA (when winds are generally lighter) compared to the Pacific where layers are rarely seen more than 30% of the time and winds are stronger year-round. The Atlantic Ocean sees fewer dry air layers than the Indian and Pacific Oceans, not simply because of the smaller extent of warm tropical ocean, but also in terms of relative distribution. Table 3 shows that the Atlantic Ocean receives more dry air parcels from continental sources; thus, one would expect to see as many or more dry air layers overall than the other two basins, as continental air is usually drier than maritime air. This discrepancy lends credence to concerns that the AIRS instrument may give artificially high values of relative humidity in the presence of high aerosol optical depths, as would be seen in dusty air from over the Sahara (S. Wong, personal communication).

- *How does the distribution of such layers vary by season?*

The seasonal distribution of midlevel dry air layers shows a wide amount of variation. In the Atlantic, most layers occur in SON, with the least in MAM. The locations of maxima appear limited to the northern Atlantic. More variation is present in the locations of maxima in the Indian Ocean, moving from the west in JJA (the active monsoon season) to the southeast in SON, with fewer layers observed in DJF and MAM. The Pacific Ocean sees many more layers in DJF, with a sharp drop-off into MAM. The

spatial distribution of layers in the Pacific also varies, though the variation is less than that in the Indian Ocean since the Pacific sees wind changes (in magnitude and direction) of a smaller scale than seen in the Indian Ocean.

- *Finally, where do these dry air layers originate, and how does this distribution vary seasonally?*

Back trajectories for all three regions suggest that most midlevel dry air layers come from the subtropics, though some variability exists. There appears to be a seasonal pattern in dry air layers, with more seen from the north in DJF and from the south in JJA, i.e., each hemisphere's respective winter. This should be expected, as the jet streams move poleward in the winter hemisphere, allowing more mixing from the midlatitudes into the tropics; an example of this was noted in Figure 37 over the TOGA COARE region. All ocean basins see trajectories from both oceanic and continental sources, although more dry air layers originate over the ocean. Some regions are the origins for different oceans depending on season (or, in the case of the Arabian Sea, provide midlevel dry air layers to all three oceans). The Atlantic and Pacific Oceans both have what appear to be jet streams from continental regions (Africa for the Atlantic, Southeast Asia for the Pacific) acting as sources of dry air.

Many questions remain with regards to midlevel dry air layers. How does the source region (i.e., oceanic versus continental) affect the layer's thickness, area, etc.? Does variation exist with respect to longer-term climatological issues, such as the El Niño-Southern Oscillation (ENSO)? Sections II-VII related dry air layers to congestus

cloud formation for January 2007; study of longer time-periods could further support these results.

CHAPTER XII

CONCLUSIONS

A proper understanding of convective clouds and their effects on the atmosphere also requires understanding the processes that limit convective development in the vertical. The strong inversion layers that mark the tops of shallow cumulus and some deep cumulonimbus clouds are easy to understand, but cannot be extrapolated to mid-level cumulus congestus clouds with cloud-tops closer to the 0°C melting layer.

This is the first study to look at observational evidence to assess two theories of congestus cloud-top height limitation. One theory looked at the changes in vertical lapse rate, dT/dp, acting as a potential cap due to increased stability in the midtroposphere. This same feature is noted in the upper troposphere, leading to a peak frequency in cloud-top heights a few kilometers below the tropopause. That being said, this study finds that there is no difference in the strength of the midtroposphere stable layer when comparing congestus and deep cloud regimes. If we are to find the reasons why certain regimes see only congestus, and not deep clouds [Kikuchi and Takayabu, 2004], we must look elsewhere.

The other theory addressed is the role of free-tropospheric dry air entraining into cloud tops, mixing the air and getting rid of a cloud's positive buoyancy. If this was the case, we would expect to find more congestus when the midtroposphere is dry, compared to deep clouds. Chapter V shows that this is the case. The mean atmospheric RH profile in the presence of congestus clouds is significantly lower than that observed

in the presence of deep clouds. Of the theories tested in this dissertation, the dry-air-entrainment theory seems to be the more plausible of the two, as the expected causes of dry-air-entrainment are noted in the observational data, whereas the expected stable-layer difference was not noted.

How prevalent are these periods of free-tropospheric dry air? Sections VIII-XI noted that very dry (RH < 20%) conditions were noted in the mid-troposphere (400-600 hPa) in 10% of the observations over the warm (i.e., convectively active) regions of the tropical oceans. The amount of variability between ocean basin and season is very apparent, lending concerns to the applicability of statistics focusing on one portion of the tropics (i.e., tropical west Pacific) to the full tropical ocean as a whole. Most areas of dry air were found to be last saturated over the ocean, though the Atlantic Ocean saw the highest percentage of land-sourced dry air layers.

As stated in discussion chapters VII and XI, this should be considered a preliminary study into the causes of congestus cloud-top limitation and the prevalence of midtropospheric dry-air layers. As larger and more accurate data sets become available, these questions can be better answered with regard to a number of phenomena (such as relation to ENSO, SST sensitivity, etc.). Future studies will help bridge the gap of our understanding of free-tropospheric humidity and its role in the tropical oceans' climate.

REFERENCES

Bowman, K. P. (1993), Large-scale isentropic mixing properties of the Antarctic polar vortex from analyzed winds, *J. Geophys. Res.*, *98*, D12, 23013-23027.

Brown, R. G., and C. Zhang (1997), Variability of midtropospheric moisture and its effect on cloud-top height distribution during TOGA COARE, *J. Atmos. Sci.*, *54*, 2760-2774.

Casey, S. P. F., A. E. Dessler, and C. Schumacher (2007), Frequency of tropical precipitating clouds as observed by the Tropical Rainfall Measuring Mission Precipitation Radar and ICESat/Geoscience Laser Altimeter System, *J. Geophys. Res.*, *112*, D14215, doi:10.1029/2007JD008468.

Casey, S. P. F., A. E. Dessler, and C. Schumacher (2009), Five-year climatology of midtroposphere dry air layers in warm tropical ocean regions as viewed by AIRS/Aqua, *J. Appl. Met. Clim.*, 48, 1831-1842.

Ciesielski, P.E., R. H. Johnson, P. T. Haertel, and J. Wang (2003), Corrected TOGA COARE sounding humidity data: Impact on diagnosed properties of convection and climate over the warm pool, *J. Clim.*, *16*, 2370-2384.

Daoud, B. A., E. Sauquet, M. Lang, C. Obled, and G. Bontron (2009), Comparison of 850-hPa relative humidity between ERA-40 and NCEP/NCAR re-analyses: detection of suspicious data in ERA-40, *Atmos. Sci. Let.*, *10*, 1, 43-47.

Dessler, A.E., and S.C. Sherwood (2000), Simulations of tropical upper tropospheric humidity, *J. Geophys. Res.*, *105*, 20,155-20,163.

Dessler, A.E., and K. Minschwaner (2007), An analysis of the regulation of tropical tropospheric water vapor, *J. Geophys. Res.*, *112*, DOI: 10.1029/2006JD007683.

European Centre for Medium-Range Weather Forecasts: ECMWF ERA-Interim Re-Analysis data, British Atmospheric Data Center, 2009-, http://data-portal.ecmwf.int/data/d/interim_daily.

Fetzer, E. J., A. Eldering, E. F. Fishbein, T. Hearty, W. F, Irion, and B. Kahn, 2005: Validation of AIRS/AMSU/HSB core products for data release version 4.0. *JPL*, D-31448, 60 pp.

Galewsky, J., A. Sobel, and I. Held, 2005: Diagnosis of subtropical humidity dynamics using tracers of last saturation. *J. Atmos. Sci.*, *62*, 3353-3367.

Jensen, M. P., and A. D. Del Genio (2006), Factors limiting convective cloud-top height at the ARM Nauru Island climate research facility, *J. Clim. 19*, 2105-2117.

Johnson, R. H., P. E. Ciesielski, and K. A. Hart (1996), Tropical inversions near the 0°C level, *J. Atmos. Sci*., *53*, 1838-1855.

Johnson, R. H., T. M. Richenbach, S. A. Rutledge, P. E. Ciesielski, and W. H. Schubert (1999), Trimodal characteristics of tropical convection, *J. Clim.*, *12*, 2397-2418.

Kalnay, E., and Coauthors (1996), The NCEP/NCAR 40-Year Reanalysis Project, *Bull. Amer. Meteor. Soc.*, *77*, 437-471.

Khairoutdinov, M., and D. Randall (2006), High-resolution simulation of shallow-to-deep convection transition over land, *J. Atmos. Sci.*, *63*, 3421-3436.

Kikuchi, K. and Y.N. Takayabu, 2004: The development of organized convection associated with the MJO during TOGA COARE IOP: Trimodal characteristics. *Geophys. Res. Lett., 31*, 10, L10101.

Kuang, K. M., and C. S. Bretherton (2006), A mass-flux scheme view of a high-resolution simulation of a transition from shallow to deep cumulus convection, *J. Atmos. Sci., 63*, 1895-1909.

Liebmann, B., and C.A. Smith (1996), Description of a complete (interpolated) outgoing longwave radiation data set, *Bull. Amer. Meteor. Soc., 77,* 1275-1277.

Luo, Z., G. Y. Liu, and G. L. Stephens (2008), CloudSat adding new insight into tropical penetrating convection, *Geophys. Res. Lett.*, 35, L19819, doi:10.1029/2008GL035330.

Luo, Z., G. Y. Liu, G. L. Stephens, and R. H. Johnson (2009), Terminal vs. transient cumulus congestus: a cloudsat perspective, *Geophys. Res. Lett., 36*, L05808, doi:10.1029/2008GL036927.

Madden, R. A. and P. R. Julian, 1994, Observations of the 40-50-day tropical oscillation—a review, *Mon. Wea. Rev., 122*, 814-837.

Mapes, B., S. Tulich, J. Lin and P. Zuidema, 2006: The mesoscale convection life cycle: Building block or prototype for large-scale tropical waves? *Dyn. Atmos. Oceans*, doi:10.1016/j.dynatmoce.2006.03.003.

Mapes, B. E. (1993), Gregarious tropical convection, *J. Atmos. Sci., 50,* 13, 2026-2037.

Parsons, D. B., K. Yoneyama, and J. L. Redelsperger, 2000: The evolution of the tropical western Pacific atmosphere-ocean system following the arrival of a dry intrusion. *Quart. J. Rot. Meteor. Soc.*, **126**, 517-548.

Pierrehumbert, R. T. (1995), Thermostats, radiator fins, and the local runaway greenhouse, *J. Atmos. Sci.*, *52*, 1784-1806.

Raymond, D. J., and A. M. Blyth (1992), Extension of the stochastic mixing model to cumulonimbus clouds, *J. Atmos. Sci.*, *49*, 1968-1983.

Redelsperger, J. L., D. B. Parsons, and F. Guichard (2002), Recovery processes and factors limiting cloud-top height following the arrival of a dry intrusion observed during TOGA COARE, *J. Atmos. Sci.*, *59*, 2438-2457.

Riehl, H. (1954), *Tropical Meteorology*, New York (McGraw-Hill), 1954.

Ryoo, J. M., D. W. Waugh and A. Gettleman (2008) Variability of subtropical upper tropospheric humidity, *Atmos. Chem. Phys.*, *8*, 2643-2655.

Simpson, J. (1992), Global circulation and tropical cloud activity, *The Global Role of Tropical Rainfall*, J. S. Theon et al., Eds., A. Deepak Publishing, Hampton, VA, 77-92.

Spencer, R. W. and W. D. Braswell (1997) How dry is the tropical free troposphere? Implications for global warming theory, *Bull. Amer. Met. Soc.*, *78*, 1097-1106.

Stephens, G. L., et al. (2002), The cloudsat mission and the a-train—A new dimension of space-based observations of clouds and precipitation, *Bull. Amer. Met. Soc.*, *83*, 1771-1790.

Tian, B., D. E. Waliser, E. J. Fetzer, B. H. Lambrigtsen, Y. L. Yung, and B. Wang, 2006, Vertical moist thermodynamic structure and spatial-temporal evolution of the MJO in AIRS observations, *J. Atmos. Sci.*, *63*, 2462-2485.

Waugh, D. W. and B. M. Funatsu (2003), Intrusions into the tropical upper troposphere: three-dimensional structure and accompanying ozone and OLR distributions, *J. Atmos. Sci*., *60*, 637-653.

Waugh, D. W. and L. M. Polvani (2000), Climatology of intrusions into the tropical upper troposphere, *Geophys. Res. Let.*, *27*, 3857-3860.

Webster, P. J. and R. Lukas (1992), TOGA COARE: The Coupled Ocean-Atmosphere Response Experiment, *Bull. Amer. Meteor. Soc.*, *73*, 1377-1416.

Yoneyama, K., and D. B. Parsons, 1999: A proposed mechanism for the intrusion of dry air into the Tropical Western Pacific region. *J. Atmos. Sci.*, *56*, 1524-1546.

Yuter, S. E., and R. A. Houze (1995), Three-dimensional kinematic and microphysical evolution of Florida cumulonimbus. Part II: frequency distribution of vertical velocity, reflectivity, and differential reflectivity, *Mon. Wea. Rev.*, *123*, 1941-1963.

Zachariasse, M., H. G. J. Smit, P. F. J. van Velthoven, and H. Kelder (2001), Cross-tropopause and hemispheric transports into the tropical free troposphere over the Indian Ocean, *J. Geophys. Res.*, *106*, 28441-28552.

Zhang, C., B. E. Mapes, and B. J. Soden (2003), Bimodality in tropical water vapour, *Q. J. Roy. Met. Soc.*, *129*, 2847-2866.

Zuidema, P. (1998), The 600-800-mb minimum in tropical cloudiness observed during TOGA COARE, *J. Atmos. Sci.*, *55*, 2220-2228.

Zuidema, P., B. Mapes, J. Lin, C. Fairall, and G. Wick (2006), The interaction of clouds and dry air in the eastern tropical Pacific, *J. Climate*, *19*, 4531-4544.

VITA

Name:	Sean Patrick Casey
Address:	Department of Atmospheric Sciences, Texas A&M University, 3150 TAMU, College Station, TX 77843-3150
Email Address:	scasey@ariel.met.tamu.edu
Education:	B.S., Atmospheric Sciences, University of Washington, 2005 M.S., Atmospheric Sciences, Texas A&M University, 2007 Ph.D., Atmospheric Sciences, Texas A&M University, 2009